nature communications

Article

https://doi.org/10.1038/s41467-026-73428-y

Regional heterogeneity in phenotypic and genetic associations between bone and brain in humans

Received: 2 May 2025

Accepted: 9 May 2026

Published online: 25 May 2026

Check for updates

Lei Zhao[1,2,7], Yilan Tang[1,2,7], Wenhui Zhao[3,7], Shijiani Li[1,2], Jie Chen[1,2], Tian Ge[4,5,6] & Yiheng Tu[1,2]

The co-occurrence of skeletal and neuropsychiatric disorders suggests underlying bone-brain associations, yet their characterization remains limited by the anatomical and biological complexity of both systems. Here, we systematically examine these associations across diverse anatomical locations using structural imaging and genetic data from approximately 45,000 UK Biobank participants. We identify widespread structural associations between bone and brain, with 34.9% of examined pairs showing significant relationships. These associations display pronounced regional heterogeneity, with effect size variation aligning with gradients of cortical development and evolutionary expansion, as well as spatial distributions of GABA and 5HT-1b receptors and gene expression profiles of oligodendrocyte precursor cells and astrocytes. Genetic analyses spanning genome-wide, pathway, locus, and single-variant levels further reveal shared genetic architecture between skeletal and brain structures, as well as with multiple neuropsychiatric and neurological traits. Enrichment within the Wnt signaling pathway highlights a potential mechanistic axis underlying bone-brain coupling, while distinct skeletal regions exhibit differential genetic links to specific brain-related health outcomes. Together, these findings demonstrate that bone-brain associations are pervasive yet exhibit substantial anatomical and genetic heterogeneity, providing a systems-level framework for understanding the shared biology of skeletal and brain health.

Bone serves as the structural backbone of the mammalian body, supporting physical form, enabling locomotion[1], and acting as a key site for hematopoiesis[2] and a reservoir for essential minerals[3,4]. Beyond these traditional roles, bone is increasingly recognized as a dynamic endocrine organ that interacts with other bodily systems to maintain overall homeostasis and health[5–7]. Growing evidence points to a complex relationship between bone and brain, often conceptualized at the molecular level as the bone-brain axis, which encompasses shared biological signaling pathways (e.g., the Wnt pathway[8–10]), interconnected neural circuits[7,11,12], and bidirectional molecular communication[13–16]. Epidemiological studies further highlight the relevance of bone-brain associations by demonstrating consistent

[1]State Key Laboratory of Cognitive Science and Mental Health, Institute of Psychology, Chinese Academy of Sciences, Beijing, China. [2]Department of Psychology, University of Chinese Academy of Sciences, Beijing, China. [3]Leonard Davis School of Gerontology, University of Southern California, Los Angeles, CA, USA. [4]Psychiatric and Neurodevelopmental Genetics Unit, Center for Genomic Medicine, Massachusetts General Hospital, Boston, MA, USA. [5]Center for Precision Psychiatry, Department of Psychiatry, Massachusetts General Hospital, Boston, MA, USA. [6]Stanley Center for Psychiatric Research, Broad Institute of MIT and Harvard, Cambridge, MA, USA. [7]These authors contributed equally: Lei Zhao, Yilan Tang, Wenhui Zhao. e-mail: tge1@mgh.harvard.edu; yihengtu@gmail.com

https://doi.org/10.1038/s41467-026-73428-y

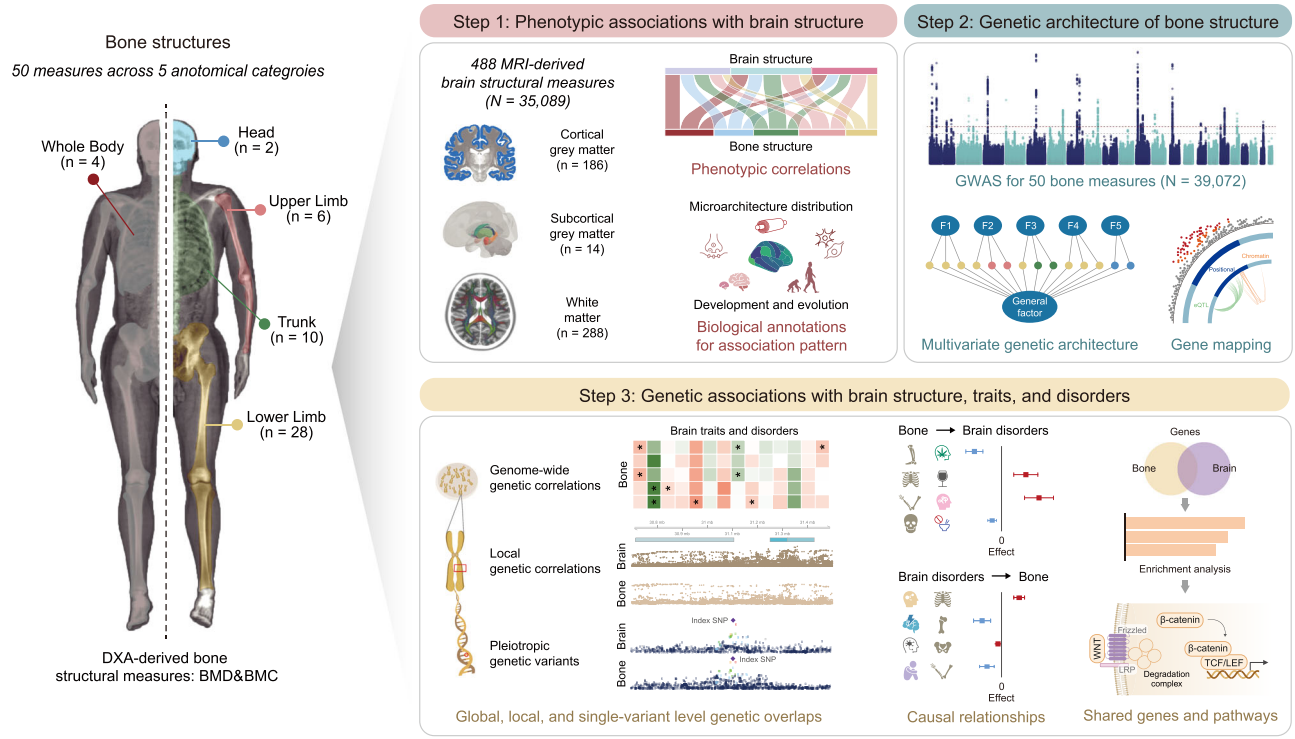

Fig. 1 | Overview of the study design. The study was conducted in three steps. First, associations between 50 dual-energy X-ray absorptiometry (DXA)-derived bone measures and 488 magnetic resonance imaging (MRI)-derived brain structure measures were quantified, and the resulting spatial patterns across the cortex were examined. These patterns were biologically annotated to explore potential mechanisms underlying the observed regional gradients. Second, the genetic architecture of the 50 bone measures was characterized, and their latent factor structure was derived using multivariate analyses. Third, genetic associations between bone measures and brain-related structural features, traits, and disorders were evaluated at genome-wide, pathway, locus, and single-variant levels, followed by enrichment analyses of overlapping genes to investigate their potential biological mechanisms. The DXA schematic is adapted from UKB example images. BMC bone mineral content, BMD bone mineral density, GWAS genome-wide association studies.

comorbidity between skeletal disorders and central nervous system conditions[17–23].

Anatomical alterations in both the skeletal system and the brain have played pivotal roles in human evolution[24,25]. The human skeleton, consisting of over 200 bones situated in diverse anatomical locations, varies in load-bearing demands, muscle mass and types[26], vessel density and blood supply[27,28], and innervation[29]. Bones in different anatomical locations also show varying susceptibilities to skeletal disorders, with certain injuries closely linked to specific conditions[30,31]. Similarly, the brain exhibits considerable anatomical complexity, characterized by regional variations in vessel density and blood supply[32], blood-brain barrier properties[33], the distribution of cell types and neurotransmitter receptors[34], and endocrine regulation[35]. Brain regions also differ markedly in their susceptibility to neurological and psychiatric disorders[36–38]. Despite the recognized importance of anatomical complexity and diversity, their role in shaping bone-brain associations remains largely unexplored. While recent animal research has shed light on the bone-brain axis[13,15], a comprehensive understanding of how bone and brain relate to one another in humans remains a formidable challenge.

Advances in imaging technologies, such as dual-energy X-ray absorptiometry (DXA) and magnetic resonance imaging (MRI), have enabled non-invasive measurement of human bone and brain structures across diverse anatomical locations, facilitating reliable assessment of their associations in large-scale datasets. Importantly, image-derived structural measures are highly heritable[39,40], holding promise to offer valuable insights into the biological pathways underlying bone-brain associations. Recent genome-wide association studies (GWAS) have characterized the genetic architecture of cortical and subcortical regions[41,42], as well as white matter tracts[43]. Leveraging these findings, numerous studies have revealed genetic correlations and shared risk variants between brain structures and disorders affecting other bodily systems[44–46]. However, the genetic architecture of bone structures across different anatomical locations remains poorly understood, leaving a gap in our knowledge regarding the genetic basis of bone-brain associations and its role in disease.

With the growing availability of large-scale biobank datasets, such as the UK Biobank (UKB)[47], we now have an unprecedented opportunity to explore the bone-brain associations by integrating phenotypic and genetic data across fine-grained bone and brain structures (Fig. 1). In this study, we examine the relationships between bone and brain in approximately 45,000 UKB participants using both imaging and genetic data. By leveraging multi-modal imaging data, we first identify extensive phenotypic associations between structural measures of bone and brain across various anatomical locations. The strength of these associations varies across cortical regions, reflecting differences in cortical microarchitecture and the evolutionary hierarchy of human brain function. We then conduct GWAS on bone structural measures and

identify anatomical location-specific genetic overlaps between bone and brain structures, as well as brain-related traits and disorders, across genome-wide, pathway, locus, and single-variant levels. Finally, we highlight the key role of the canonical Wnt signaling pathway in mediating these bone-brain associations.

Results

Overview for imaging measures

This study included 50 DXA-derived bone structural measures and 488 MRI-derived brain structural measures to investigate bone-brain associations (Supplementary Data 1). The selection of these

measures was guided by anatomical relevance and biological function. Among the 50 bone measures, 23 assessed bone mineral content (BMC) and 27 assessed bone mineral density (BMD), both widely used to characterize bone structure and closely linked to musculoskeletal disorders[48–50]. Although related, these measures capture distinct biological properties: BMC reflects total mineral mass and is influenced by bone size and growth, whereas BMD reflects mineral concentration per unit volume and is more closely related to bone quality, microstructure, and metabolic activity. All bone measures were grouped into five anatomical categories: head ($n = 2$), trunk ($n = 10$), upper limb ($n = 6$), lower limb ($n = 28$), and whole body ($n = 4$).

The 488 brain measures were divided into ten categories based on anatomical location and imaging modality, including subcortical volume, cortical volume, cortical surface area, cortical thickness, fractional anisotropy (FA), diffusion tensor mode (MO), mean diffusivity (MD), orientation dispersion (OD), intra-cellular volume fraction (ICVF), and isotropic volume fraction (ISOVF). These categories capture complementary neurobiological processes. For example, cortical thickness reflects radial neuronal migration and the neuronal and glial architecture within cortical columns, whereas cortical surface area is linked to tangential neuronal migration and indexes the number of mini-columnar units. In total, 14 measures quantified the volume of subcortical regions, 186 measures assessed the volume, surface area, and thickness of 62 cortical regions, and 288 measures evaluated various white matter (WM) microstructural properties (FA, MO, MD, OD, ICVF, and ISOVF) across 48 WM tracts. Further methodological details are provided in the Methods section and supplementary text.

Phenotypic bone–brain associations

We examined pairwise phenotypic correlations between the 50 bone measures and 488 brain measures, adjusting for a range of potential confounders (see "Methods" section for a complete list of covariates). In our discovery dataset, which included 35,089 white British individuals of European ancestry, we identified 8519 bone–brain associations (34.9% of examined pairs; Fig. 2A, Supplementary Figs. 1–10, and Supplementary Data 2) at the Bonferroni-corrected significance level ($p < 2.05 \times 10^{-6}$, across 50×488 tests), suggesting widespread structural connections between bone and brain. To evaluate the robustness and generalizability of these findings, we performed a replication analysis in an independent validation dataset ($N = 4257$) of non-white British Europeans. A total of 5609 associations (Supplementary Data 2) were successfully replicated with nominal significance ($p < 0.05$) and concordant effect directions.

The head showed the highest proportion of significant associations with brain measures, with 60.1% (n_{pair} = 587) of pairwise correlations exceeding the Bonferroni threshold ($p < 2.05 \times 10^{-6}$). This was followed by the trunk (41.2%, $n_{pair} = 2010$), lower limb (30.3%, $n_{pair} = 4144$), and upper limb (29.4%, $n_{pair} = 860$). In terms of correlation strength, the upper limb exhibited the strongest average correlations ($|\beta| = 0.051$), followed by the head ($|\beta| = 0.043$), trunk ($|\beta| = 0.039$), and lower limb ($|\beta| = 0.034$). These patterns indicate that bone–brain associations vary systematically across anatomical locations of the skeleton.

Among the brain measures, subcortical volumes had the highest proportion of significant associations with bone measures (63.7%; $n_{pair} = 446$), followed by cortical measures (39.6%, $n_{pair} = 3679$) and WM measures (30.5%, $n_{pair} = 4,394$). All significant correlations between bone measures and cortical volume and surface area were negative, whereas correlations with cortical thickness were primarily positive (Fig. 2B). Subcortical volumes followed a similar pattern to cortical volume, showing predominantly negative correlations with bone measures (Fig. 2C). For WM measures, all significant correlations with MD and ISOVF were negative, whereas correlations with FA were predominantly positive, indicating that higher bone mineral content and density are associated with better WM integrity (Fig. 2D). Correlations with OD were more heterogeneous, with approximately equal proportions of positive and negative associations across WM tracts. Positive correlations were primarily observed in the superior fronto-occipital fasciculus, superior cerebellar peduncle, and pontine crossing tract, while negative correlations were mainly observed in the corticospinal tract and inferior cerebellar peduncle. In summary, the proportion and direction of bone-brain associations depend strongly on both the anatomical location of the brain region and the imaging modality, highlighting a complex and regionally heterogeneous relationship between skeletal and neural structures.

Given the versatile role of the hypothalamus and its established association with bone homeostasis in animal studies[51,52], we additionally parcellated the hypothalamus into 10 subregions and found that the posterior hypothalamus exhibited the strongest associations with bone measures (Supplementary Fig. 11, Supplementary Data 3, and supplementary text).

Both brain and bone structures are influenced by sex[53,54]. To explore potential sex differences in bone-brain associations, we conducted sex-specific analyses and identified 5647 significant bone-brain pairwise correlations ($p < 2.05 \times 10^{-6}$) in females ($N = 18,193$) and 3600 significant correlations in males ($N = 16,896$; Supplementary Figs. 12–33 and Supplementary Data 4). Overall, females exhibited stronger (two-sample t-test $p < 0.001$; Supplementary Fig. 34) and more widespread bone–brain correlations compared to males. To further assess whether age gradients may have influenced these sex-specific findings, participants were stratified into younger (<60 years) and older (≥60 years) groups within each sex. Association analyses were repeated within each stratum, and heterogeneity between strata was assessed using Cochran's Q test. No significant heterogeneity was observed among females and only one heterogeneous pair (FDR $q < 0.05$) was detected among males (Supplementary Data 5), indicating that the observed sex differences in bone–brain associations are unlikely to be substantially confounded by age-related effects.

Microarchitecture and evolution patterns underlying bone-brain associations

The strength of bone-brain correlations varies substantially across cortical regions (Fig. 2 and Supplementary Data 2). For example, the average correlation between bone measures and cortical surface area is more than fourfold stronger in the left parahippocampal cortex ($|\beta| = 0.067$) compared to the left cuneus ($|\beta| = 0.015$). Similarly, the average correlation with cortical thickness in the left rostral anterior cingulate cortex ($|\beta| = 0.053$) is approximately threefold greater than that in the left insular cortex ($|\beta| = 0.014$). Cortical microarchitecture plays a crucial role in regulating morphological variability, as it profoundly influences brain metabolism, neural plasticity, and susceptibility to disorders[55,56].

To investigate the biological factors contributing to the variation in bone-brain correlation strength across cortical regions (Fig. 2B), we examined 30 spatial distribution maps (Supplementary Fig. 35 and Supplementary Data 6) that capture different aspects of cortical microarchitecture. These included 19 maps related to neurotransmitter receptors or transporters, 7 maps for cell-type-specific gene expression, and 4 maps for microstructure features[56]. After accounting for spatial autocorrelation using surrogate maps[57], we found significant correlations between the spatial distribution of $GABA_a$ ($r = 0.611$, $p = 2 \times 10^{-4}$) and 5HT-1b ($r = 0.449$, $p = 1.5 \times 10^{-3}$) neurotransmitter receptors and the cross-regional variability in the strength of correlations between cortical surface area and bone measures, after applying a 5% false discovery rate (FDR) correction (Fig. 2E and Supplementary Data 7). For cortical thickness, significant correlations were observed with the spatial distribution of cell type-specific gene expression in oligodendrocyte precursors ($r = 0.614$, $p = 2 \times 10^{-4}$) and astrocytes ($r = 0.611$, $p < 1 \times 10^{-4}$), as well as with myelin microstructure ($r = -0.559$, $p = 3.8 \times 10^{-3}$) and $GABA_A$ neurotransmitter

https://doi.org/10.1038/s41467-026-73428-y

receptors ($r = -0.463$, $p = 3.6 \times 10^{-3}$). Together, these results show that macroscopic bone–brain structural correlations exhibit a spatial gradient that aligns with microscopic patterns of neurotransmitter receptor distribution and cellular composition.

Considering the unique evolutionary specializations in humans and the rapid growth of both the brain and bone during development[24,58,59], we also explored how brain evolution and developmental expansion may shape the regional variability of bone-brain connection strength (Supplementary Fig. 35 and Supplementary Data 6). Our results (Fig. 2F and Supplementary Data 7) demonstrated that the regional variability of cortical surface area and thickness was positively associated with their functional evolutionary hierarchy ($r = 0.553$, $p = 7 \times 10^{-4}$) and developmental expansion ($r = 0.498$, $p = 1 \times 10^{-4}$), suggesting that evolutionary and developmental processes may also influence regional differences in bone–brain communication.

Fig. 2 | Phenotypic associations between bone and brain. A Manhattan plot of pairwise phenotypic correlations between bone and brain measures. Each dot represents a pairwise correlation (linear regression model, two-sided test). The *x* axis shows brain measures, with colors indicating different bone categories. The red dashed line represents the Bonferroni-corrected significance threshold (raw $p < 2.05 \times 10^{-6}$). **B** Regional variation in bone-brain correlation strength for cortical regions, with colors indicating the average correlation strength for each region across bone measures. **C** Regional variation in bone–brain correlation strength for subcortical regions, with colors indicating the average correlation strength for each region across bone measures. **D** The top five brain measures with the strongest average correlations across bone measures within each category of WM. **E** Bar chart illustrating the spatial correlations (Pearson correlation, two-sided test, $n = 62$ for both cortical surface area and cortical thickness) between the regional variability in cortical microarchitecture distribution and the strength of the association between cortical surface area (top) or thickness (bottom) and bone measures. **F** Bar chart illustrating the spatial correlations (Pearson correlation, two-sided test, $n = 62$ for both cortical surface area and cortical thickness) between brain developmental and evolutionary maps and the strength of the association between cortical surface area (left) or thickness (right) and bone measures. Different colors represent different types of brain maps. Asterisks indicate significant associations at the 5% FDR level. All statistical tests were two-sided. B bilateral; FA fractional anisotropy, ICVF intracellular volume fraction, ISOVF isotropic volume fraction, L left, MD mean diffusivity, MO diffusion tensor mode, OD orientation dispersion, OPC oligodendrocyte precursors, R right.

The genetic architecture of bone measures

To comprehensively characterise the genetic basis of bone-brain associations, we first examined the genetic architecture of 50 DXA-derived bone measures by conducting GWAS in a cohort of 39,072 white British individuals of European ancestry. This analysis identified 1767 independent [linkage disequilibrium (LD) $r^2 < 0.1$] genome-wide significant bone-single nucleotide polymorphism (SNP) associations (Supplementary Figs. 36–85 and Supplementary Data 8) across 393 unique genetic loci (Fig. 3A and Supplementary Data 9) at a Bonferroni-corrected threshold of $p < 1 \times 10^{-9}$ ($5 \times 10^{-8}/50$). These included 7 novel loci that did not overlap with previously reported suggestive associations ($p < 5 \times 10^{-6}$; 1 for BMD, 6 for BMC; Supplementary Data 10), as well as 18 loci that did not overlap with genome-wide significant signals ($p < 5 \times 10^{-8}$) reported in prior GWAS of bone mineral traits (10 for BMD and 11 for BMC, with 3 overlapping between BMD and BMC; Supplementary Data 11)[40,60–63]. Of the 393 unique loci, 351 did not overlap with genome-wide significant variants for skeletal proportions reported in a recent study[24], suggesting limited genetic overlap between bone mineral measures and skeletal proportions.

Among the five categories of bone measures, the head and lower limb showed the highest degree of genetic specificity (Fig. 3A), with most of their independently associated variants being unique to these categories. This finding provides genetic evidence for the molecular basis of anatomical differentiation within the skeletal system. The linkage disequilibrium score regression (LDSC)[64] intercepts for all 50 bone measures were close to 1 (mean intercept = 1.021, range = 0.993–1.043; Supplementary Data 12), suggesting that genomic inflation can be largely attributed to polygenicity rather than confounding factors. Additionally, we conducted sex-specific GWAS for male and female participants (Supplementary Data 13), which revealed highly consistent genetic effects at genome-wide significant loci across sexes (Pearson's $r = 0.965$; Supplementary Fig. 86).

To explore whether genetic signals are shared across ancestries, we sought to replicate our GWAS findings using three independent datasets from the UKB: a non-white British cohort of European individuals ($N = 4720$), an East Asian cohort (UKBEAS, $N = 214$), and an African cohort (UKBAFR, $N = 381$). Of the 1767 independent significant bone–SNP associations, 830 (46.97%, spanning 199 loci) reached nominal significance ($p < 0.05$) with consistent effect directions in the non-white British European cohort (Supplementary Data 14). In the non-European cohorts, 139 associations (across 57 loci) reached nominal significance in UKBEAS, and 126 associations (across 37 loci) were nominally significant in UKBAFR. The lower replication rates in non-European cohorts likely reflect both reduced statistical power due to smaller sample sizes and ancestry-specific genetic architecture.

We estimated SNP-based heritability (h^2) for each of the 50 bone measures using LDSC[64]. At the Bonferroni-corrected significance level ($p < 1 \times 10^{-3}$, across 50 tests), significant heritability was observed for all bone measures, with an average h^2 of 29.17% (range = 20.67–43.55%; Fig. 3B and Supplementary Data 15). Among the five anatomical categories of bone measures, the head showed the highest average h^2 (mean $h^2 = 42.9\%$), followed by the whole body (34.2%), trunk (30.7%), upper limb (28.4%), and lower limb measures (27.1%). Notably, while there was a moderate correlation (Pearson's $r = 0.541$, $p = 5.07 \times 10^{-5}$), h^2 for bone measures was significantly higher in males compared to females (mean $h^2 = 31.28\%$ in males vs. 24.86% in females; $p = 2.25 \times 10^{-9}$, two-sample *t*-test; Supplementary Figs. 87–89 and Supplementary Data 15). Heritability estimates obtained using GCTA-GREML[65] were on average slightly higher but highly correlated with LDSC estimates (Pearson's $r = 0.894$, $p < 0.001$; Supplementary Data 15 and Supplementary text). Additionally, we calculated pairwise genetic correlations among 46 local bone measures (excluding the four whole-body measures) and found strong positive correlations across measures (mean $r_g = 0.733$, range = 0.325–0.993; Supplementary Fig. 90 and Supplementary Data 16).

Before exploring the genetic overlap between bone and brain measures, we sought to determine whether categorizing bone measures by anatomical locations accurately represents their genetic similarity. To this end, we applied genomic structural equation modeling (Genomic SEM)[66] to generate a low-dimensional latent representation of 46 local bone measures based on their pairwise genetic correlation estimates. A full description of the model selection procedure is provided in the Methods section. Rather than using the five anatomical categories, the best-fitting model was a bifactor model with one general factor and five specific genomic factors (F1–F5) (Fig. 3C, Supplementary Fig. 91, and Supplementary Data 17), as evidenced by its excellent fit [$\chi^2(df = 943) = 931{,}651$, AIC = 931,927, CFI = 0.991, SRMR = 0.042]. In this model, the general factor positively loaded on all measures, accounting for an average of 70% of the genetic covariation. Genomic factor F5 aligned with the head region, and F3 encompassed all trunk-related measures, consistent with anatomical groupings. However, notable divergences emerged in the limb measures. Specifically, measures of the lower leg and upper limb clustered together under F2, whereas femoral BMD/BMC measures formed a distinct factor (F1). BMC of the femur neck and Ward's triangle loaded onto F4, with the remaining lower limb measures assigned to F1. These patterns revealed biologically coherent clusters of genetic covariation that do not strictly follow anatomical boundaries.

The divergence between F1 (femur-dominant) and F2 (upper limb and lower leg) is biologically interpretable. F2 appears to represent a functional genetic module linked to pathways involved in dynamic mechanical loading and high-frequency muscle contraction. Upper-limb bones exhibit BMD/BMC variation driven largely by localized muscle traction and fine-motor use, while lower leg bones experience high strain rates and torsional stress during activities such as running, jumping, or rapid directional movements. These dynamic forces differ fundamentally from the predominantly static axial loading that characterizes femoral BMD/BMC variation, which is captured by F1. Thus, F2 likely reflects shared genetic determinants of adaptive bone remodeling under dynamic, muscle-driven mechanical stimuli, whereas F1 captures genetic pathways associated with load-bearing axial compression. Given that the bifactor model provides a parsimonious and more accurate representation of the genetic similarities among bone measures, we subsequently used the latent genomic

https://doi.org/10.1038/s41467-026-73428-y

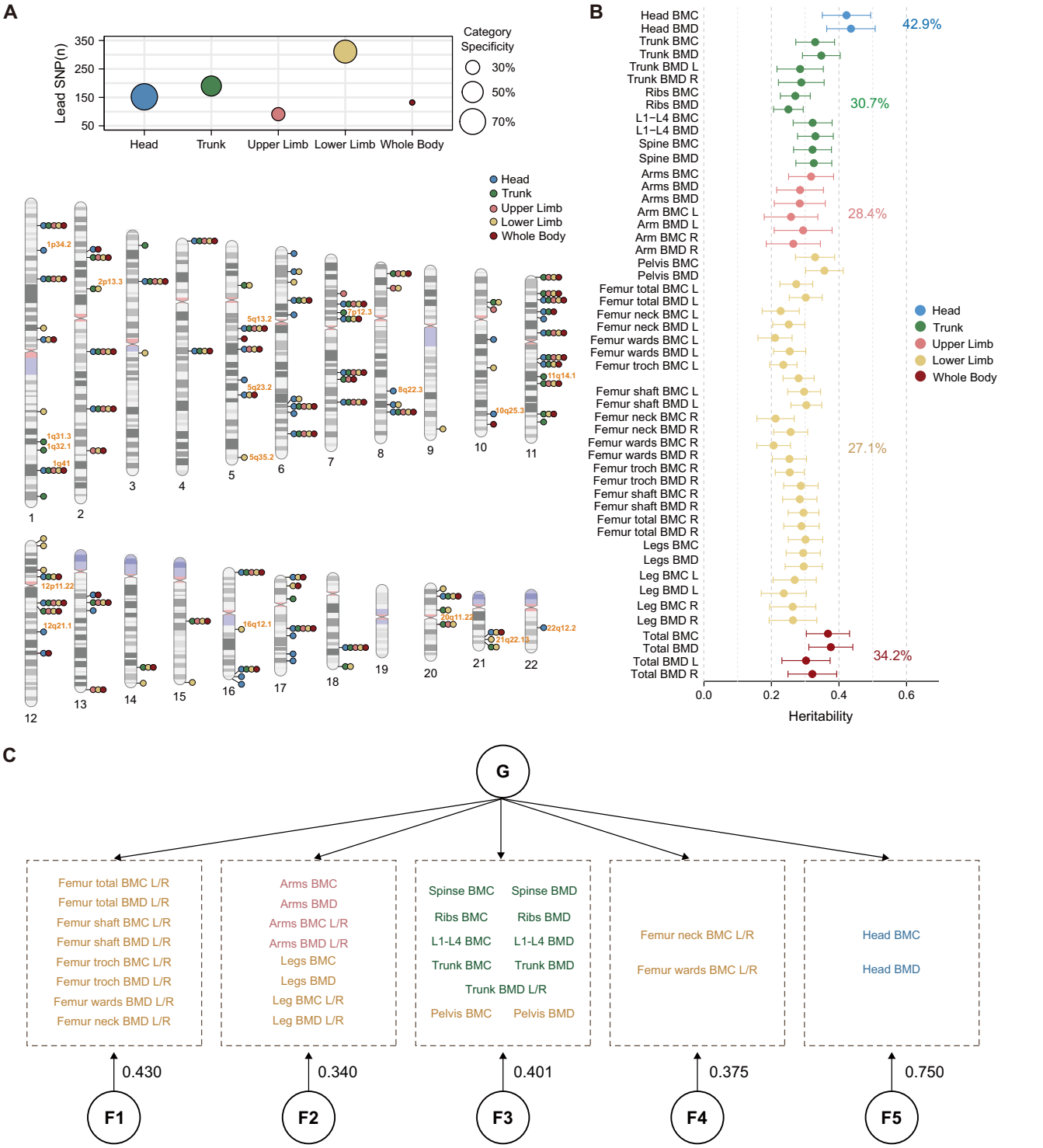

Fig. 3 | The genetic architecture of bone measures. A Top: the number of lead single-nucleotide polymorphisms (SNPs) identified by FUMA for each bone measure category. The size of each circle represents the proportion of category-specific associations, calculated as the ratio of category-specific lead SNPs to the total number of lead SNPs for that category. Bottom: ideogram displaying genome-wide significant loci associated with 50 bone measures ($p < 1 \times 10^{-9}$). Genomic regions containing previously unreported loci at genome-wide significance ($p < 5 \times 10^{-8}$) are indicated with orange labels. Colors indicate different bone categories. **B** SNP-based heritability for 50 bone measures, grouped into anatomical categories and color-coded accordingly (see Supplementary Data 1 and the underlying GWAS summary statistics for details of the bone measures). Points represent heritability estimates, and error bars indicate 95% confidence intervals based on the standard errors of the estimates. The average heritability of each category is shown. **C** A bifactor genomic SEM model illustrating the genetic covariance structure of bone measures. Genomic factors are represented as circles, and one-headed arrows indicate the average standardized loadings of these factors on bone measures. The text color for each bone measure corresponds to its anatomical category. BMC bone mineral content, BMD bone mineral density, F factor, G general factor, L left, R right.

factors, rather than anatomical categories, to explore the genetic relationships between bone and brain.

GWAS on the six genomic factors identified 21 loci that were not detected among the 50 bone measures (Supplementary Fig. 92 and Supplementary Data 18), indicating that these latent factors capture shared genetic components across bone measures and substantially enhance discovery power. To move from variant-level associations toward biological interpretation, we performed gene- and pathway-level analyses. Gene-level association analysis using MAGMA[67] revealed 230 unique genes ($p < 5.23 \times 10^{-8}$, $50 \times 19{,}110$ tests; Supplementary Data 19) associated with bone measures, corresponding to 1726 significant bone–gene pairs. For the latent genomic factors, 112 unique genes ($p < 4.41 \times 10^{-7}$, across $6 \times 18{,}909$ tests; Supplementary Data 20) were identified, corresponding to 123 significant factor-gene pairs. In parallel, using FUMA positional mapping, expression quantitative trait locus (eQTL) mapping, and chromatin interaction mapping, we identified 510 unique genes associated with bone measures (Supplementary Data 21), 324 of which were not captured by MAGMA, indicating additional regulatory mechanisms beyond proximity-based assignment.

In the MAGMA gene-set enrichment analyses, 225 unique Gene Ontology (GO) gene sets exhibited significant enrichment for at least one bone measure at the 5% FDR level (Supplementary Data 22). These gene sets mainly involved processes related to morphogenesis, development, differentiation, and remodeling of multiple tissues, as well as pathways such as Wnt signaling and metabolic regulation. Similar gene sets and enrichment patterns were observed when using a ±10 kb annotation window size (Supplementary Data 23 and S24). Partitioned LDSC analysis of tissue and cell types[68] revealed significant enrichments for bone measures in active gene regulatory regions across multiple tissues, including bone, muscle, cardiovascular system, and nervous system at the 5% FDR level (Supplementary Data 25). Additional enrichment analysis of the latent genomic factors can be found in supplementary text (Supplementary Data 26 and S27).

Genome-wide genetic correlations between bone and brain

Emerging evidence suggests a link between bone health and various physiological, psychological, and neurodegenerative conditions[69]. To investigate the genetic underpinnings of these associations, we used cross-trait LDSC[70] to estimate genome-wide genetic correlations between 50 bone measures and 70 complex traits and disorders (Supplementary Data 28). After applying a 5% FDR correction, we identified significant genetic correlations spanning physiological conditions, personality traits, cognitive functions, food preferences, musculoskeletal disorders, neurodegenerative disorders, and psychiatric disorders (Fig. 4A, Supplementary Fig. 93, and Supplementary Data 29). As anticipated, osteoporosis showed significant negative correlations with all bone measures, with the most pronounced effect in right trunk BMD ($r_g = -0.818$). Body mass index (BMI) showed positive correlations with bone measures across all genomic factors, particularly in the legs ($r_g = 0.176$). Additionally, the intensity of physical activity was positively correlated with bone measures from genomic factors F2, F3, and F4 (max $r_g = 0.164$ in the legs). We also observed widespread positive genetic correlations between musculoskeletal disorders and bone measures, including knee osteoarthritis (max $r_g = 0.277$ in the legs), spinal stenosis (max $r_g = 0.344$ in the lumbar spine L1-L4), hip osteoarthritis (max $r_g = 0.285$ in the femur neck), and meniscus derangement (max $r_g = 0.224$ in the legs).

Both positive and negative genetic correlations were observed between bone measures and brain disorders. Significant positive correlations were found with bipolar disorder (BD), Parkinson's disease (PD), Lewy body dementia (LBD), attention deficit hyperactivity disorder (ADHD), obsessive-compulsive disorder (OCD), and alcohol dependence. In contrast, significant negative correlations were identified with insomnia, Alzheimer's disease (AD), anxiety disorder (ANX), and multiple sclerosis (MS). In addition, these brain disorders exhibited distinct genetic correlation patterns across anatomical locations of bone measures (Fig. 4A, B). For example, ADHD showed significant correlations with bone measures from both genomic factors F2 and F3, while BD and ANX were exclusively associated with F1. PD was correlated with bone measures across F1, F2, and F5, whereas MS was associated solely with F2. Notably, some brain-related traits demonstrated opposing correlations across different genomic factors. For instance, intelligence and educational attainment were positively correlated with bone measures in F5, but negatively correlated with F2 and F3. Taken together with the phenotypic findings, these results suggest an inherent organizational principle linking skeletal and neural systems.

To further explore the genetic overlap between bone measures and physical and mental health, we conducted polygenic risk scores (PRS) analysis[71]. As a sanity check, PRS derived from the discovery GWAS of the 50 bone measures significantly predicted their respective phenotypes in an independent cohort of non-white British Europeans, explaining a mean incremental phenotypic variance (R^2) of 4.13% (range = 0.59–14.23%; Supplementary Fig. 94 and Supplementary Data 30), with 14 bone measures having an R^2 greater than 5%. We then evaluated the association between the 50 bone PRS and 204 complex traits across multiple categories (Supplementary Data 31). At the Bonferroni-corrected significance level ($p < 4.90 \times 10^{-6}$, across 50×204 tests), we identified 54 phenotypes significantly associated with bone PRS, primarily in categories such as body composition, musculoskeletal and connective tissue disorders, pain, neurological disorders, personality traits, mental health, cognitive ability, and lifestyle (Fig. 4C). For instance, bone PRS predicted cognitive ability and educational attainment, aligning with our findings from the genome-wide genetic correlation analysis. Additionally, higher PRS for several bone measures were associated with better mental health outcomes, including lower levels of depression, anxiety, and neuroticism. Elevated PRS were also linked to greater warmth and sociability, as well as lower levels of diligence and nervousness. Finally, we observed associations between bone PRS and various lifestyle factors, including sleep, smoking, and physical activity. Full details, including the strength and direction of associations, are provided in Supplementary Fig. 95, and Supplementary Data 32. Together, these results indicate that polygenic profiles of bone extend beyond musculoskeletal traits or diseases to neurological, cognitive, and behavioral domains, showing widespread pleiotropy between skeletal and neural systems.

Local genetic correlations between bone and brain

While genome-wide genetic correlation analysis provides valuable insights into the overall genetic overlap between bone measures and brain disorders, it does not pinpoint the specific genetic factors driving these associations. We thus conducted local genetic correlation analysis to identify region-specific genetic overlaps[72]. Several brain disorders with significant genome-wide genetic correlations with bone measures also exhibited significant local genetic associations at one or more genomic loci ($p < 9.78 \times 10^{-7}$, see "Methods" section for details on multiple testing correction; Supplementary Figs. 96–101 and Supplementary Data 33). For instance, ADHD showed positive local genetic correlations with bone measures from genomic factor F2 at loci on chromosomes 4 and 17, whereas AD demonstrated negative genetic associations with bone measures from F2 at loci on chromosome 7.

In addition, we uncovered significant local genetic correlations for bone–brain pairs that did not exhibit genome-wide genetic correlations (Supplementary Figs. 102–105 and Supplementary Data 33). Specifically, post-traumatic stress disorder displayed positive genetic correlations with genomic factors F2 and F3 at loci on chromosomes 8 and 11. Major depressive disorder (MDD) showed significant negative associations with F1, F3, and F4 at loci on chromosomes 5 and 6. Schizophrenia demonstrated negative associations with all genomic

https://doi.org/10.1038/s41467-026-73428-y

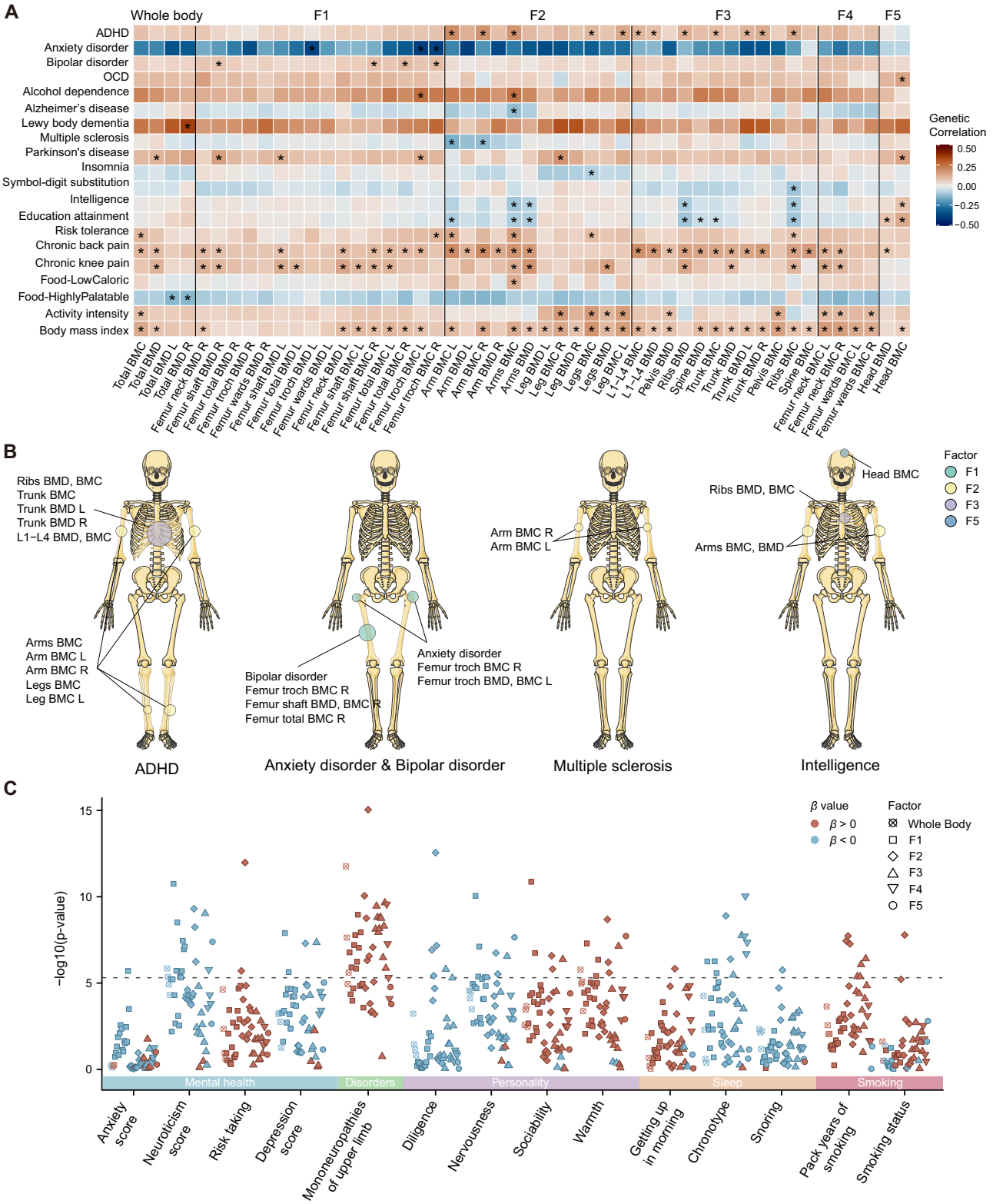

factors except F5 at loci on chromosomes 6 and 15, while showing positive associations with F1 and F2 at loci on chromosomes 4, 8, and 10. Furthermore, cannabis use disorder (CUD) showed significant negative associations with F1 and F4 at loci on chromosome 8.

In parallel with the phenotypic correlation analysis between bone and brain, we assessed both global and local genetic correlations between 50 bone DXA measures and 488 brain MRI measures. While no significant genome-wide genetic correlations were identified, we uncovered 519 significant region-specific genetic correlations across multiple genomic loci ($p < 1.17 \times 10^{-6}$, see "Methods" section for details on multiple testing correction; Fig. 5A, Supplementary Fig. 106–115, Supplementary Data 34 and 35), suggesting that shared genetic components are concentrated within specific genomic regions rather than broadly distributed across the genome. Notably, the superior temporal region, transverse temporal region, and corticospinal tract showed significant local genetic correlations with bone measures across all

Fig. 4 | Selected genome-wide genetic correlations between bone measures and complex traits and disorders. A Heatmap showing selected genetic correlations between 50 bone measures and 70 complex traits or disorders. The colors represent the magnitude of genetic correlations, and asterisks indicate significant associations at the 5% FDR level. **B** Illustration of the anatomical location of bone measures that exhibit significant genetic correlations with attention deficit hyperactivity disorder (ADHD), anxiety disorder, bipolar disorder, multiple sclerosis and intelligence. Schematic skeleton images are provided by Servier Medical Art (https://smart.servier.com), licensed under CC BY 4.0 (https://creativecommons.org/licenses/by/4.0/). **C** Significance plot showing selected associations between PRS of the 50 bone measures and complex phenotypes. The *x* axis shows specific phenotypes, with box colors indicating their category domains. The color of the marker indicates the direction of the association (red: positive associations; blue: negative associations). The shape of the marker corresponds to different bone genomic factors. The dashed line represents the Bonferroni-corrected significance threshold (raw $p < 4.90 \times 10^{-6}$). All statistical tests were two-sided. BMC bone mineral content, BMD bone mineral density, F factor, Food-Highly Palatable food preference for highly palatable, Food-LowCaloric food preference for low caloric, L left; OCD obsessive-compulsive disorder, R right.

latent genomic factors, indicating a widespread genetic overlap with the skeletal system. Consistent with the phenotypic findings, most local genetic correlations were negative for cortical volume, cortical surface area, ISOVF, and MD, and positive for FA. Moreover, the corticospinal tract showed the greatest number of significant associations with bone measures at both phenotypic (501 pairs, Supplementary Data 2) and genetic levels (170 pairs, Supplementary Data 34), suggesting that the observed phenotypic associations may, in part, reflect shared genetic influences.

Functional enrichment of genes related to both bone and brain

To further localize the genetic variants underlying both global and local genetic correlations between bone and brain, we examined genome-wide significant SNPs associated with the 50 bone measures in the NHGRI-EBI GWAS catalog[73]. This analysis identified variants associated with both bone measures and a wide range of complex traits and disorders, including cognitive performance, education, brain structure and function, psychological traits, personality, smoking behavior, neurodegenerative and neuropsychiatric disorders, sleep disorders, anthropometric traits, musculoskeletal disorders, and various conditions related to the immune, endocrine, and cardiovascular systems (Supplementary Data 36).

We then performed enrichment analyses on the genes (Supplementary Data 37) harboring overlapping genetic signals between bone measures and brain-related traits or disorders to elucidate the biological mechanisms underlying bone-brain associations. At the 5% FDR level, our analysis revealed significant enrichments (Supplementary Fig. 116 and Supplementary Data 38) in several Gene Ontology (GO) terms related to the canonical Wnt signaling pathway, chondrocyte differentiation, and embryonic morphogenesis. Additionally, we identified several significant Kyoto Encyclopedia of Genes and Genomes (KEGG) terms, with the Wnt signaling pathway again emerging as the most prominent (Supplementary Data 38).

To evaluate whether these enrichments were driven by genes harboring putative causal variants, we repeated the enrichment analyses using genes prioritized through fine-mapping. The results were highly consistent with the primary analysis, and the canonical Wnt signaling pathway remained the most significantly enriched term (Supplementary Data 39 and S40). In total, we identified nine genes involved in the canonical Wnt signaling pathway (*WNT4*, *WNT2B*, *CSNK1G3*, *WNT16*, *SOX7*, *LGR4*, *LRP4*, *LRP5*, *AXIN1*), along with eight additional genes (*BDNF*, *TNFRSF11B*, *RUNX2*, *SOX6*, *GDF5*, *ESR1*, *GATA4*, *HDAC5*) that either regulate signaling modules within this pathway or act as downstream effectors (Supplementary Fig. 117 and supplementary text). Collectively, these enrichment results converge on the canonical Wnt signaling pathway, implying that this pathway may serve as a key axis linking bone formation and neural development.

Druggability analysis of the canonical Wnt signaling pathway

We further explored the translational potential of the 17 bone-brain overlapping genes involved in the canonical Wnt signaling pathway (Supplementary Fig. 117). Among these genes, 13 were classified as druggable (Supplementary Data 41 and 42) according to the Drug-Gene Interaction Database (DGIdb) and the Druggable Genome database[74], indicating known or predicted molecular features that are compatible with pharmacological targeting. Notably, DrugBank and Therapeutic Target Database annotations indicate that *BDNF* is currently under clinical investigation for neurological disorders[75,76], and *TNFRSF11B* has been reported as a potential therapeutic target in osteoarthritis[77]. We further conducted exploratory drug repurposing analyses using Gene2Drug[78] to identify candidate compounds that may modulate pathways linked to these genes. This analysis prioritized 32 compounds spanning multiple drug classes at Bonferroni-corrected significance ($p < 2.24 \times 10^{-6}$), including antimalarials, antiarrhythmics, antihypertensive agents, antipsychotic agents, antidepressants, antiepileptics, and anti-Parkinson agents (Supplementary Data 43). These findings suggest potential opportunities for pathway-level pharmacological modulation but remain exploratory and require experimental validation.

Pleiotropic genetic variants between bone and brain

To explore shared genetic signals between bone and brain, we performed Bayesian colocalization analyses[79]. We considered colocalization to be supported when the posterior probability of the shared variant hypothesis (PPH4) exceeded 0.8. Our analysis revealed multiple regions with high colocalization probabilities between bone and brain measures (Supplementary Data 44). For example, both global brain volume (PPH4 = 0.973; Fig. 5B) and total cortical surface area (PPH4 = 0.865; Supplementary Fig. 118) showed strong evidence of shared association signals with bone measures in the 11p14.1 region. Additional colocalized signals were observed in the 6q22.32 region for the middle frontal gyrus, lateral orbitofrontal cortex, and caudal anterior cingulate cortex (PPH4 > 0.977; Supplementary Figs. 119–121).

Beyond structural brain features, Bayesian colocalization analysis further supported widespread genetic pleiotropy between bone measures and various personality traits and cognitive phenotypes. For example, variants within the 8p23.1 region were associated with both arm BMC and neuroticism (PPH4 = 0.950; Supplementary Fig. 122). In the 1q32.1 region, spine BMC colocalized with executive function (PPH4 = 0.925; Supplementary Fig. 123). Reaction time colocalized with multiple bone measures within the 11p11.2 region, including head BMC (PPH4 = 0.921; Supplementary Fig. 124), spine BMD (PPH4 = 0.910; Supplementary Fig. 125), and femur neck BMD (PPH4 = 0.947; Supplementary Fig. 126). In this same region, additional colocalization was observed between smoking behavior and head BMD (PPH4 = 0.812; Supplementary Fig. 127), femur wards BMC (PPH4 = 0.986; Supplementary Fig. 128), and total body BMD (PPH4 = 0.850; Supplementary Fig. 129). In the 6p22.1 region, pelvis BMD was linked to both MDD (PPH4 = 0.888; Fig. 5B) and worry (PPH4 = 0.880; Supplementary Fig. 130). Lastly, we found shared genetic influences between bone measures and several musculoskeletal disorders (Supplementary Fig. 131-S134, Supplementary Data 44, and supplementary text).

Causal relationships between bone and brain disorders

In light of the extensive genetic associations between bone structure and brain disorders, we applied Mendelian Randomization (MR) analysis[80] to explore their putative causal relationships. We evaluated bidirectional causal effects between 50 bone measures and 20 brain

https://doi.org/10.1038/s41467-026-73428-y

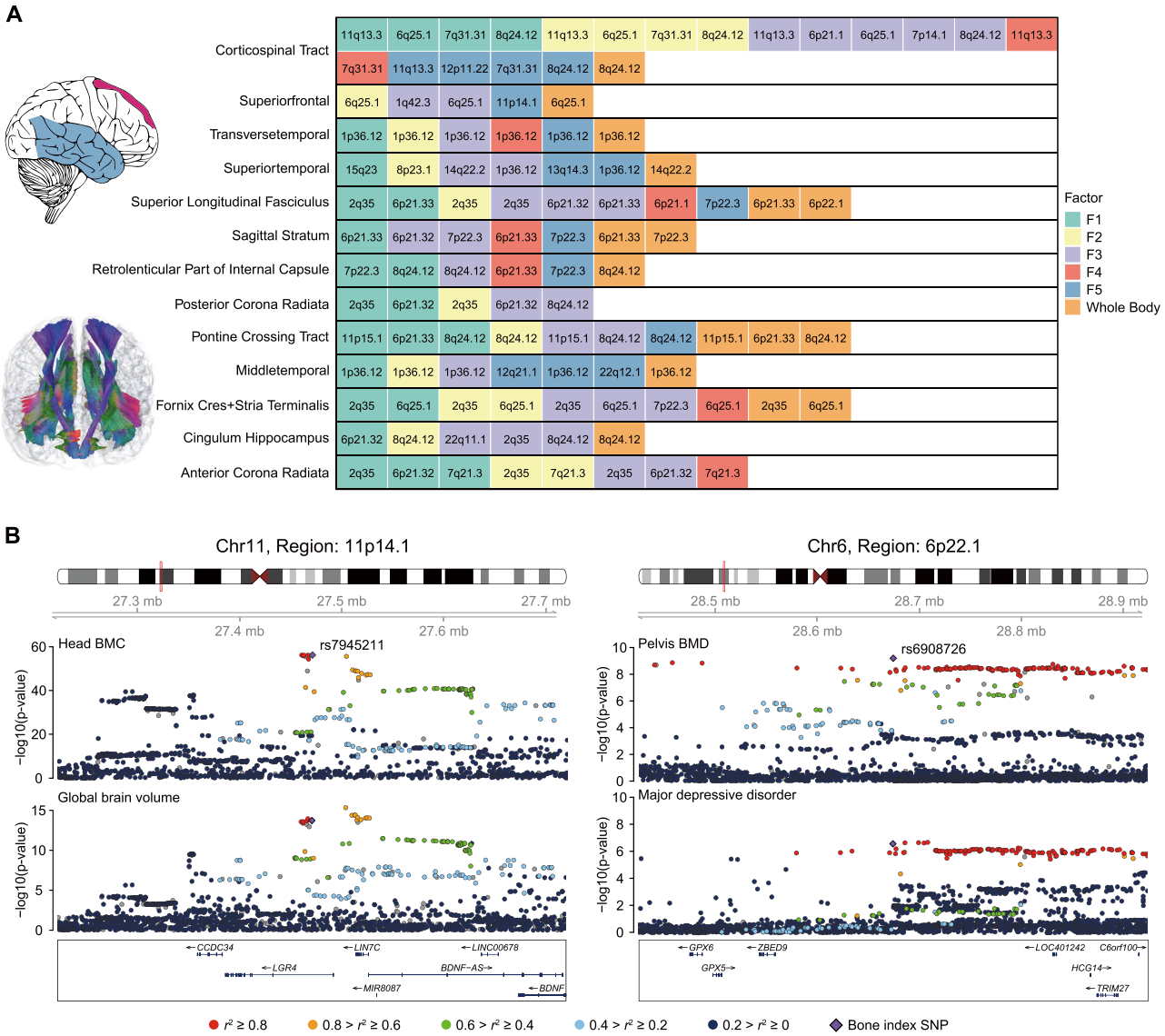

Fig. 5 | Local genetic correlations and selected genetic pleiotropy between bone and brain measures. A Local genetic correlation between brain regions or white matter tracts and bone measures across multiple genomic loci. Only brain regions or WM tracts with more than five significant local genetic correlations (Bonferroni-corrected significance; raw $p < 1.17 \times 10^{-6}$; two-sided) are displayed. The text within the matrix cells denotes the genomic regions where brain measures exhibit significant local genetic correlations with bone measures. Brain schematics were generated by cerebroViz (https://ethanbahl.github.io/cerebroViz/). **B** Examples of genetic pleiotropy between bone measures, brain structure, and brain-related disorders. Within the 11p14.1 region (left), a genetic locus is associated with both head bone mineral content (BMC) and global brain volume, with Bayesian colocalization analysis suggesting strong support for a shared causal signal [posterior probability (PPH4) = 0.973]. Within the 6p22.1 region (right), colocalization is observed between pelvis bone mineral density (BMD) and major depressive disorder (PPH4 = 0.888). Colors represent the level of linkage disequilibrium (LD, r^2) between the index SNP of the bone GWAS and neighboring variants. F factor, SNP single-nucleotide polymorphism.

disorders (Supplementary Data 45). At Bonferroni-corrected significance ($p < 5 \times 10^{-5}$), we identified several causal effects of bone measures on neuropsychiatric outcomes (Fig. 6A and Supplementary Data 46). Specifically, left leg BMC was negatively associated with the risk of CUD; bilateral trunk BMD exerted positive effects on the risk of alcohol dependence; the risk of OCD was positively influenced by total BMD, bilateral leg BMC, and right arm BMD; and the risk of AN was negatively associated with total BMD, total BMC, bilateral femur neck BMD, legs BMD, and heads BMD. Notably, genomic factor F2 showed complex, reversed effects on multiple disorders: lower BMD and BMC within this factor were associated with an increased risk of CUD and AN, but a decreased risk of OCD.

We also identified causal effects of brain disorders on bone structure at Bonferroni-corrected significance ($p < 6.68 \times 10^{-5}$; Fig. 6B and Supplementary Data 46). Specifically, we found positive causal effects of ADHD on right trunk BMD within genomic factor F3. In contrast, stroke was associated with decreased BMC of right femur wards in F4. Multiple bone structures in F1, F3, and F4 exhibited reduced BMC as a result of MS. Autism spectrum disorder (ASD) was linked to decreased whole-body BMC and BMD, with the strongest effects observed in bone structures within F2, F3, and F5. In summary, we observed bidirectional causal relationships between bone structure and brain disorders, with the magnitude and direction of these effects modulated by specific genomic factors of bone measures.

Strong concordance emerged between the causal inference results and the genetic correlation analyses. Among the 20 brain disorders evaluated in both approaches, we identified global or local

https://doi.org/10.1038/s41467-026-73428-y

A

Exposure	Category	Outcome	IVs (N)	P-value
Leg BMC L	F2	Cannabis use disorder	7	6.52×10^{-18}
Trunk BMD L	F3	Alcohol dependence	17	1.30×10^{-5}
Trunk BMD R	F3		19	4.46×10^{-7}
Total BMD	Whole body	Obsessive-compulsive disorder	65	3.81×10^{-5}
Arm BMD R	F2		14	4.15×10^{-7}
Leg BMC L	F2		7	2.07×10^{-5}
Leg BMC R	F2		10	1.37×10^{-5}
Total BMD	Whole body	Anorexia nervosa	59	3.93×10^{-8}
Total BMC	Whole body		49	3.33×10^{-5}
Femur neck BMD L	F1		40	8.69×10^{-6}
Femur neck BMD R	F1		31	3.32×10^{-9}
Legs BMD	F2		42	3.86×10^{-5}
Head BMD	F5		67	2.11×10^{-5}

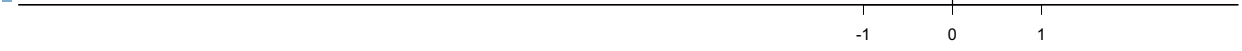

B

Exposure	Category	Outcome	IVs (N)	P-value
Attention deficit hyperactivity disorder	F3	Trunk BMD R	23	1.79×10^{-6}
Stroke	F4	Femur wards BMC R	4	1.29×10^{-5}
Multiple sclerosis	F1	Femur total BMC L	64	1.42×10^{-6}
	F3	Spine BMC	72	1.12×10^{-5}
	F3	Pelvis BMC	74	3.95×10^{-5}
	F4	Femur neck BMC L	74	5.20×10^{-6}
	F4	Femur wards BMC L	77	1.68×10^{-5}
Autism spectrum disorder	Whole body	Total BMD	2	4.37×10^{-6}
	Whole body	Total BMC	2	4.75×10^{-6}
	Whole body	Total BMD L	2	9.25×10^{-6}
	F2	Arms BMD	2	7.67×10^{-8}
	F2	Arm BMD R	2	3.90×10^{-6}
	F2	Arm BMD L	2	4.15×10^{-6}
	F2	Arm BMC R	2	2.76×10^{-5}
	F3	Spine BMD	2	1.45×10^{-7}
	F3	Trunk BMD	2	5.47×10^{-6}
	F3	Trunk BMC	2	2.16×10^{-5}
	F3	L1-L4 BMC	2	3.00×10^{-5}
	F5	Head BMD	2	1.97×10^{-5}

Fig. 6 | Causal relationships between bone measures and brain disorders. **A** Forest plot illustrating significant putative causal effects of bone measures on brain disorders that passed Bonferroni correction (raw $p < 5 \times 10^{-5}$). **B** Forest plot illustrating significant putative causal effects of brain disorders on bone measures that passed Bonferroni correction (raw $p < 6.68 \times 10^{-5}$). Points represent causal effect estimates (raw β), and error bars indicate 95% confidence intervals. Statistical estimates were obtained using fixed-effect IVW for two or three independent variants (IVs) and multiplicative random-effects IVW when more than three IVs are available. Only effect estimates that consistently show the same direction across IVW and nine additional MR methods, and are significant in at least one of these methods, are considered significant. Brain disorder GWAS data sources and details are provided in Supplementary Data 45. The color of the boxes on the *y* axis corresponds to genomic factors of bone measures. All *P* values were derived from two-sided tests. BMC bone mineral content, BMD bone mineral density, F factor, L left, R right.

bone-brain genetic correlations involving 11 disorders (Supplementary Data 29 and S33). Of these, five associations were additionally supported by MR (Supplementary Data 46). Notably, four of the five causal relationships exhibited effect directions consistent with their corresponding genetic correlations, with positive associations for alcohol dependence, OCD, and ADHD, and negative associations for MS.

Robustness and sensitivity analyses were conducted to evaluate the potential impact of weak instrument bias and horizontal pleiotropy. Instrumental strength was examined using the mean *F*-statistic for each set of instrumental variables (IVs), and for all significant associations the mean *F*-statistic exceeded 30 (Supplementary Data 46), indicating that weak instrument bias was unlikely to

dramatically affect the causal estimates. We additionally performed multivariable Mendelian randomization (MVMR)[81] to estimate the direct effects of bone measures on brain disorders, while accounting for potential pleiotropic pathways operating through metabolic, inflammatory, and gut microbiota factors. Across the 1439 factors examined, the significant causal relationships remained robust after adjustment ($p < 0.05$), although some effect sizes were modestly attenuated (Supplementary Data 47).

Discussion

Recent studies have increasingly recognized the importance of the skeletal system in overall health, providing substantial evidence for bone–brain associations[82,83]. However, existing research has often overlooked how anatomical complexity and diversity contribute to regional variations in function and susceptibility across both bone and brain. In this study, we performed a comprehensive analysis of bone-brain associations in approximately 45,000 UK Biobank participants, identifying a total of 8519 phenotypic associations that were disproportionately distributed across different anatomical categories of bone and brain. We further characterized the genetic architecture of bone structures across diverse anatomical locations, identifying seven novel genetic loci. Through genome-wide, pathway, locus and single-variant level analyses, we revealed both shared and distinct genetic overlaps between different anatomical categories of bone structures and a range of brain-related traits and disorders.

Research on bone-brain associations has typically focused on how bone-derived signals influence specific brain regions (e.g., the hippocampus)[16,84], or how brain-derived signals impact skeletal homeostasis or specific bones (e.g., the femur)[13,85]. Our findings not only identified widespread in vivo bone–brain associations, but also revealed that the presence and strength of these associations are shaped by anatomical complexity and diversity. For example, the head exhibited the highest proportion of associations with the brain, approximately 1.5 times greater than the trunk, while the upper limb demonstrated the strongest overall associations. Additionally, subcortical brain regions exhibited a higher proportion of associations with bone than cortical regions and WM, consistent with animal studies that highlight the pivotal role of subcortical regions, particularly the hypothalamus, in bone remodeling and health[13,86]. Within the hypothalamus, our analysis further revealed heterogeneous associations across subregions, with the posterior hypothalamus, a key regulator of sympathetic responses and energy balance[7,87], exhibiting the strongest associations with bone.

More broadly, the strength of bone–brain associations varied across cortical and subcortical regions, forming a graded distribution from strong to subtle effects. Given the large sample size, even modest associations likely capture true but small-scale biological coupling. This spatial gradient may thus reflect underlying organizational principles of bone–brain communication. Supporting this interpretation, we found that the spatial variation in association strength across cortical regions correlated with gradients of $GABA_A$ and 5HT-1b receptor density, suggesting distributed bone–brain associations and implicating neurotransmitter systems involved in neuronal excitability, synaptic transmission, and neuropsychiatric disorders[88–91]. Previous studies suggested that GABAergic circuits and brain-derived serotonin regulate bone metabolism[14,52,92], while bone-derived hormone osteocalcin can in turn modulate these neurotransmitters[16,93]. Our findings thus underscore the importance of accounting for anatomical complexity and diversity in future research and suggest that neurochemical signaling may partially mediate the effects of anatomical complexity on bone-brain associations.

Interestingly, higher BMD/BMC was associated with reduced cortical surface area and volume but increased cortical thickness, which may reflect distinct neurobiological processes underlying cortical surface area and thickness. According to the radial unit hypothesis of cortical expansion, the extent and timing of neurogenesis and migration of neurons from the embryonic proliferative zone differentially shape cortical thickness and surface area[94]. These developmental pathways may be further influenced by genetic factors. Consistent with this framework, large-scale imaging-genetics studies have demonstrated a strong genetic correlation between cortical volume and surface area, but little to no genetic correlation between surface area and cortical thickness[95]. This implies that cortical volume is primarily driven by surface area rather than thickness, providing a potential explanation for why cortical volume and surface area showed similar directions of association with bone measures, whereas cortical thickness largely showed the opposite pattern. Additionally, BMD or BMC was positively associated with white matter FA and negatively associated with MD and ISOVF measures. Although these effects differ in statistical sign, their biological implications are consistent: higher FA together with lower MD and ISOVF reflect greater WM integrity, including more coherent axonal organization, reduced extracellular free water, and preserved myelination[96].

Although previous studies have identified numerous genetic signals associated with BMD and BMC[40,60–62,97,98], it remains unclear whether these genetic signals vary across anatomical locations. In our large-scale GWAS of BMD and BMC, we identified 393 independent genetic loci across 50 bone measures, including 7 novel loci and 18 that did not reach genome-wide significance in previous studies. These loci exhibited both shared and distinct genetic associations across anatomical locations, with the head and lower limb showing highly location-specific signals. Additionally, the bifactor model, which classified bone measures into one general and five specific genomic factors, provided a more accurate representation of the genetic relationships among bone measures compared with traditional anatomical categories. Notably, leg measures in the lower limb were genetically more similar to upper limb measures than to femur measures within the same anatomical categories, likely reflecting shared functional demands. Both the upper limb and legs undergo repetitive, dynamic mechanical loading during daily activities, such as walking, running, and lifting, leading to similar bone remodeling processes driven by overlapping genes.

Clinical research has established a strong relationship between bone structure and a wide range of brain-related traits or disorders[69,99–101]. Our study reinforced this connection by revealing both genome-wide and local genetic correlations. The genetic correlation patterns were largely consistent with our phenotypic findings, suggesting that bone-brain associations are influenced by genetic predispositions.

Moreover, MR analysis identified bidirectional causal effects between bone measures and brain disorders, indicating that bone structure may influence the risk of psychiatric conditions, while neurodevelopmental and neurodegenerative disorders may, in turn, affect bone health. Notably, our findings challenge the traditional view that higher BMD or BMC invariably protects brain health[102,103]. Instead, increased BMD or BMC may, in certain cases, elevate the risk of specific disorders, such as alcohol dependence and OCD. Although the underlying mechanisms remain unclear, one possible explanation is that bone-derived hormones differentially regulate brain regions with varying susceptibility to neurological and psychiatric disorders, a pattern reflected in the phenotypic and genetic bone-brain associations identified in our study. Mechanistic interpretations will require further validation through studies that integrate bone-derived biomarkers, region-specific gene expression, and clinical outcomes. Overall, disruption of the complex and dynamic interactions between bone and brain, where abnormalities in either system impair bidirectional communication, may have broad consequences for overall health[103–107]. A holistic understanding of these interactions is critical for developing timely prevention and targeted intervention strategies to maintain both skeletal and brain function.

The genes harboring shared genetic signals between bone measures and brain structures or disorders were primarily enriched in the canonical Wnt signaling pathway or involved in its regulation. This developmental pathway is essential for controlling bone formation and maintaining bone homeostasis, while also playing a pivotal role in dendritic arborization, neurotransmission, and synaptic plasticity in the brain[8]. Recent animal studies have provided compelling evidence that dysregulated Wnt signaling underlies both bone disorders and neurodegenerative diseases[15,108–110], and our findings further supported its conserved role in bone-brain connections. We also identified shared genes central to autophagy, including *ATG13* and *AMBRA1*. Autophagy is essential for maintaining cellular homeostasis and has been implicated in both neurodegenerative diseases and osteoclast-mediated bone remodeling. Moreover, autophagy interacts with key developmental pathways, particularly the canonical Wnt signaling pathway, to coordinate proliferative responses[111]. Together, these results indicate that bone-brain connections may be governed by a complex regulatory network, in which Wnt signaling and other biological pathways are integrally linked to maintain cellular homeostasis and coordinate the development and function of both skeletal and neural systems.

Our findings provide several potential clinical and translational implications. First, standard bone density indicators could serve as early, accessible markers for neuropsychiatric risk, as skeletal alterations in specific anatomical regions correspond to distinct brain-disorder profiles. Future work could explore whether integrating routine skeletal screening with neuropsychiatric risk assessment could improve early detection. Second, since both low and high bone density were associated with elevated risk for different brain disorders, defining an optimal, health-promoting range for bone metabolism across the lifespan emerges as an important goal. Third, although shared pathways identified in our analyses, such as Wnt signaling, suggest possible biological intersections between bone and brain, direct therapeutic translation remains speculative. For example, while BDNF supports both neuronal function and bone formation[112–114], its relevance as a therapeutic target in bone-brain contexts is unknown and will require systematic experimental validation. Finally, future research should prioritize elucidating the molecular mediators of cross-system communication, employing longitudinal designs and multi-omics integration to map how perturbations in one system propagate to the other.

Several limitations should be considered when interpreting our findings. First, while BMD and BMC are routinely measured in clinical settings and serve as established indicators of bone health[50], they may not fully capture the multifaceted characteristics of bone. Future research should consider incorporating additional measures relevant to bone health, such as skeletal proportions. Second, the cross-sectional design of this study limits our ability to capture dynamic changes in bone and brain across the lifespan. Both systems undergo continuous development, remodeling, and degeneration, and their interplay may be characterized by key milestones or transitional phases that are challenging to identify through cross-sectional analysis. Longitudinal studies are thus essential to uncover these milestones and provide insights into the temporal dynamics of bone-brain associations. Third, our interpretations of the biological mechanisms underlying bone–brain associations are constrained by the limitations of the reference knowledge bases. Further exploration and validation are needed, particularly regarding how environmental factors modulate genetic effects. Finally, our cross-ancestry replication analyses were exploratory and limited by small sample sizes in the non-European cohorts. As a result, we cannot fully distinguish the relative contributions of reduced statistical power and ancestry-specific genetic effects. Larger non-European cohorts will be essential to systematically characterize the shared and ancestry-specific genetic factors.

In summary, this study represents a comprehensive in vivo characterization of bone-brain associations, revealing how anatomical complexity and heterogeneity shape their relationship. Our analysis highlights the critical involvement of genetic predisposition and cortical microarchitecture in shaping these associations, offering novel insights into the mechanisms linking the two systems with greatly improved anatomical and genomic resolutions. These findings enhance our understanding of the comorbidity between physical and mental health and hold the potential for guiding the development of future inter-organ therapeutic strategies aimed at addressing bone and brain disorders.

Methods

Participants

All individual-level data used in the current study were obtained from the UK Biobank (UKB) under application ID 71901 (https://www.ukbiobank.ac.uk). Ethical approval for UKB was granted by the North West Multi-Centre Research Ethics Committee. All participants provided informed consent at recruitment. The UKB is a prospective population-based study comprising approximately 500,000 individuals recruited across Great Britain. All participants provided written informed consent. During the initial assessment stage (2006–2010), all participants visited one of the assessment centers, where demographics, health-related outcomes, and biological samples were collected. A subset of approximately 50,000 participants was invited to follow-up imaging assessments starting in 2014, which included dual-energy X-ray absorptiometry (DXA) and magnetic resonance imaging (MRI) scans. This study primarily used genotype data from the baseline visit and bone DXA and brain MRI data from the imaging visit.

Bone and brain imaging measures

Both whole-body and location-specific bone mineral density (BMD) and bone mineral content (BMC) levels were measured using an iDXA instrument (GE-Lunar, Madison, WI). See https://biobank.ndph.ox.ac.uk/showcase/ukb/docs/DXA_explan_doc.pdf for detailed information on the acquisition procedure. We included 50 quality-controlled DXA measures provided by the UKB, comprising 23 BMC and 27 BMD measures, each with a sample size exceeding 20,000. BMC represents the total mineral content within the scanned bone area, while BMD is calculated by dividing the BMC by the area size. These measures were anatomically categorized into five groups (Supplementary Data 1): head ($n = 2$), trunk ($n = 10$), upper limb ($n = 6$), lower limb ($n = 28$), and whole body ($n = 4$).

We used quality-controlled T1-weighted structural MRI (sMRI) and diffusion MRI (dMRI) data collected by the UKB. Brain images were acquired using a Siemens Skyra 3 T scanner, equipped with a standard Siemens 32-channel RF receive head coil. All data were preprocessed by the UKB brain imaging team. Detailed information on imaging acquisition and processing is available on the UKB website (http://biobank.ctsu.ox.ac.uk/crystal/refer.cgi?id=2367; https://biobank.ndph.ox.ac.uk/showcase/showcase/docs/brain_mri.pdf). In this study, we included 488 brain structural measures categorized into ten groups: cortical volume ($n = 62$), cortical surface area ($n = 62$), cortical thickness ($n = 62$), subcortical volume ($n = 14$), fractional anisotropy (FA; $n = 48$), diffusion tensor mode (MO; $n = 48$), mean diffusivity (MD; $n = 48$), orientation dispersion (OD; $n = 48$), intra-cellular volume fraction (ICVF; $n = 48$), and isotropic volume fraction (ISOVF; $n = 48$). The 186 sMRI-derived cortical measures, calculated using the FreeSurfer tool, represent three morphological features (surface area, thickness, and volume) of 62 cortical regions anatomically defined by the Desikan–Killianny–Tourville (DKT) atlas[115]. Fourteen sMRI-derived subcortical measures capture the volume of 14 subcortical regions segmented with the FMRIB's Integrated Registration and Segmentation tool (FIRST)[116]. 288 dMRI-derived white matter (WM) measures,

extracted using tract-based spatial statistics (TBSS) analysis, characterize six different properties of 48 WM tracts anatomically defined by the Johns Hopkins University (JHU) atlas (ICBM-DTI-81)[117].

Phenotypic bone–brain associations

To investigate the phenotypic associations between bone and brain, we performed pairwise linear regression for each pair of bone DXA and brain MRI measures, treating bone measures as independent variables and brain measures as dependent variables. The primary analysis was conducted using a discovery dataset comprising 35,089 white British individuals of European ancestry [Field-ID (FID) 22006] as determined by genetic principal component analysis (FID 21000). An independent validation dataset, comprising 4257 non-white British Europeans, was used to replicate the significant bone-brain phenotypic associations identified in the discovery dataset[118].

For all pairs, we adjusted for the effects of sex, age, age squared, sex-by-age interactions, sex-by-age squared interactions, total brain volume, the volumetric scaling factor from T1-weighted head images to standard space, and several anthropometric measures (height, sitting height, weight, hip circumference, waist circumference, body mass index, and lean body mass). Additionally, we included covariates for the presence of disability or infirmity, overall health rating, history of long-standing illness, smoking status, drinking frequency, Townsend deprivation index, assessment center location, and the position of the brain in the scanner. We also adjusted for the top 40 genetic principal components (PCs) provided by the UKB to account for potential population stratification. For each variable in the linear regression, outliers, defined as values outside four standard deviations from the mean, were removed from the analysis. Continuous variables were standardized to facilitate interpretation, and categorical variables were coded as dummy variables. Significant bone-brain association pairs were reported at the Bonferroni-corrected significance level ($p < 2.05 \times 10^{-6}$, across 50×488 tests).

Annotations of cortical microarchitecture

To explore the biological mechanisms underlying cross-regional variability in the strength of associations between cortical surface area or thickness and bone measures, we examined their spatial correlations with the cross-regional variability in cortical microarchitecture. We focused on cortical surface area and thickness measures in this analysis, as these metrics are largely orthogonal and key determinants of cortical volume.

We utilized 30 cortical microarchitecture maps that represent the spatial distribution of neurotransmitter receptors and transporters, cortical microstructure, and cell type-specific gene expression patterns, sourced from previous studies (see Supplementary Data 6 for details). These maps were derived from various modalities, including MRI scans, positron emission tomography (PET), and microarray data. Specifically, we included 19 maps of neurotransmitter receptors and transporters across nine neurotransmitter systems: serotonin (5-HT1a, 5-HT1b, 5-HT2a, 5-HT4, 5-HT6, 5-HTT), dopamine (D1, D2, DAT), norepinephrine (NET), acetylcholine (α4β2, M1, VAChT), histamine (H3), cannabinoid (CB1), opioid (MOR), glutamate (mGluR5, NMDA), and GABA (GABAa). When multiple maps for the same neurotransmitter receptor or transporter were available, they were averaged into a single map, weighted by the sample size of each dataset. We also incorporated microstructure maps, including cortical myelin (a proxy measure derived from the T1w/T2w ratio of MRI), the first PC of gene expression, the first PC of neurotransmitter receptors and transporters, and synapse density. We included cell type-specific gene expression maps for seven cell types: astrocytes, endothelial cells, microglia, oligodendrocyte precursors, excitatory neurons, inhibitory neurons, and oligodendrocytes. These maps were generated by averaging the expression levels of gene markers preferentially expressed in each cell type (see Supplementary Data 48 for details on cell-specific gene markers). The gene markers were curated from five single-cell transcriptomic studies[119–123] conducted on human postmortem cortical samples, ensuring robustness by minimizing biases associated with acquisition methodologies, analytical processes, or thresholding criteria. A detailed description can be found in the study by Seidlitz and colleagues[124]. The expression levels of genes were derived from the Allen Human Brain Atlas (AHBA), a transcriptional atlas developed by the Allen Institute[125]. The AHBA consists of 3702 spatially distributed tissue samples collected from the brains of six healthy adult donors with no history of psychiatric or neuropathological disorders. Gene expression data were preprocessed using the abagen toolbox[126] following standard procedures. First, probes were filtered to distinguish true expression signals from background noise, excluding those with intensities below the background threshold in ≥50% of samples across donors. For genes indexed by multiple probes, the probe demonstrating the most consistent pattern of regional variation across donors was retained. To enhance spatial coverage, right hemisphere samples were reflected to their contralateral position in the left hemisphere, and vice versa, when necessary, given minimal lateralization in microarray gene expression[125]. Samples were assigned to brain regions defined by the DKT atlas if their MNI coordinates fell within 2 mm of a given region. For brain regions without any assigned samples, expression values were imputed using the nearest tissue sample based on Euclidean distance. Inter-donor variability was addressed by normalizing the expression values across genes using a robust sigmoid function, followed by min-max normalization across samples matched to the same brain region. Finally, samples assigned to the same brain region were averaged separately for each donor and then across donors, yielding an expression matrix of 15,633 genes across 62 cortical regions.

We averaged the 50 bone–brain correlation coefficients for each cortical region, resulting in a region-wise map ($n_{region} = 62$) that captures the cross-regional variability in the strength of association between bone and brain. The microarchitecture maps were transformed into the same coordinate space using the neuromaps package[55]. We then assessed the spatial correlations between the two (surface area and thickness) bone–brain correlation maps and the 30 microarchitecture maps using Pearson correlation analyses. Statistical significance was determined using the BrainSMASH package[57], which corrects for spatial autocorrelation by incorporating a spatially constrained null model. Specifically, we generated 10,000 surrogate brain maps matching the spatial autocorrelation pattern of the bone-brain correlation maps, and calculated the Pearson correlation between each microarchitecture map and the surrogate brain map. The p-value was defined as the proportion of surrogate-derived correlation values exceeding the empirical correlation value. We reported significant correlations at a false discovery rate (FDR) threshold of 5% (across 2 bone–brain correlation maps × 30 microarchitecture maps).

Using the same procedure, we also assessed the spatial correlations of bone-brain correlation maps with maps representing cortical expansion variability during development and evolution, as well as the evolutionary conservatism of the brain's functional hierarchy (Supplementary Data 6). Briefly, developmental cortical expansion refers to the growth of cortical surface area from term birth to adulthood, quantified by dividing the mean fractional areal map of adults by that of term infants, where the fractional areal map represents the proportion of total cortical surface occupied by each region. Evolutionary cortical expansion is defined analogously, except that the comparison is made between adult humans and nonhuman primates rather than between adults and infants. The functional evolution hierarchy reflects the evolutionary organization of the brain's functional architecture. The human cortex is organized along a hierarchical gradient, in which unimodal sensory areas progressively integrate into higher-order, transmodal regions supporting abstract and complex cognition. Regions that show a higher position in this hierarchy in humans

compared to macaques are considered to have greater functional evolutionary advancement. In general, higher-order cognitive regions exhibit higher functional evolution hierarchy scores.

Quality control for genetic data

Imputed genetic data for 488,377 participants, along with a range of quality control (QC) metrics, were obtained from the UKB (FID 22828). We restricted our analysis to white British individuals of European ancestry (FID 22006), who underwent a bone DXA scan, had fewer than ten third-degree relatives identified (FID 22021), did not have sex chromosome aneuploidy (FID 22019), and were not flagged as outliers for heterozygosity or missing rates (FID 22027). This resulted in 39,072 participants in the discovery dataset. We then removed single-nucleotide polymorphisms (SNPs) with a minor allele frequency (MAF) < 0.5%, a genotyping rate <90%, the Hardy-Weinberg equilibrium test $p < 1 \times 10^{-7}$, and imputation INFO scores <0.5.

GWAS of bone measures

Genome-wide association studies (GWAS) for the 50 bone measures were performed using REGENIE v3.2.6 (https://rgcgithub.github.io/regenie)[127]. REGENIE employs a two-step approach to account for population structure and sample relatedness. In the first step, a whole-genome regression model was built to predict the phenotype based on genotyped variants using a leave-one-chromosome-out (LOCO) strategy. The genetic predictor derived from this step was then used as an offset in the second step, where variant association analysis was performed on the imputed SNPs via standard linear regression. The covariates included in both steps were sex, age, age squared, sex-by-age and sex-by-age squared interactions, height, weight, body mass index (BMI), genotype measurement batch, and the top 40 genetic PCs provided by the UKB.

To validate our findings, we used three independent datasets, excluding relatives of the discovery sample. The first validation dataset consisted of 4720 non-white British Europeans[118]. Additionally, we validated the findings in two non-European cohorts: an East Asian cohort (UKBEAS, $N = 214$) and an African cohort (UKBAFR, $N = 381$). For all validation analyses, we adjusted for the top 10 genetic PCs.

We used LD score regression v.1.0.1 (https://github.com/bulik/ldsc)[64], with a pre-computed European LD reference panel built from the 1000 Genomes Project, excluding the major histocompatibility complex (MHC) region (chromosome 6: 25–34 Mb), to estimate the SNP-based heritability for each bone measure. We also assessed the intercept of the regression to ensure that inflation in test statistics can be largely attributed to polygenicity rather than confounding factors such as population stratification, cryptic relatedness, and model misspecification.

We used FUMA[128] v1.6.1, an online platform designed for annotating, prioritizing, and interpreting GWAS results, to identify genomic loci and perform functional annotation. SNPs with genome-wide significance were identified using a Bonferroni-corrected p-value threshold of 1×10^{-9} (across 50 bone measures), and an LD threshold of $r^2 < 0.6$. Variants in strong LD with a significant SNP were grouped into the same locus. Lead SNPs within each locus were further refined using a more stringent LD threshold of $r^2 < 0.1$. Genomic regions with distances of less than 250 kb were merged into a single locus. Loci with overlapping boundaries were merged, and the SNP with the smallest p-value within each merged locus was retained as the representative tag SNP. We compared the start and end positions of identified loci to those reported in prior GWAS[40,60–63]. A genomic locus was considered novel if its boundary did not overlap with any variants reaching a suggestive significance threshold ($p < 5 \times 10^{-6}$) in prior GWAS of bone mineral traits.

Genomic SEM

Genomic structural equation modeling (Genomic SEM) (https://github.com/GenomicSEM/GenomicSEM)[66] was used to model latent genomic factors of bone measures based on their genetic similarity. We first constructed a genetic covariance matrix for 46 local bone measures using linkage disequilibrium score regression (LDSC)[70], excluding 4 whole-body measures. Variants within the MHC region and those with imputation INFO scores below 0.9 were excluded. The estimated genetic covariance matrix was then smoothed to the nearest positive definite matrix using the Higham algorithm. The smoothed genetic covariance matrix was standardized to derive the genetic correlation matrix.

Next, we used the parallel, Kaiser, and optimal coordinates methods from the nFactors R package to determine the number of latent genomic factors that best represented the data, given the genetic correlation matrix. All three methods consistently suggested five factors. We thus conducted a five-factor exploratory factor analysis (EFA) using the Promax rotation (i.e., correlated factors) within the psych R package. We then fitted four types of confirmatory factor analysis models using Genomic SEM. The first model was a common factor model, in which all measures loaded onto a single factor. The second model consisted of five correlated factors. Individual measures were assigned to a factor if their standardized loading exceeded 0.5. Measures with loadings below 0.5 on all factors were assigned to the factor with the highest standardized loading. No measure had loadings greater than 0.5 across multiple factors, eliminating the need for cross-factor loadings. The third model was a bifactor model, which included a general factor capturing the shared variation across all measures, alongside five specific factors learned from the second model to account for covariation not explained by the general factor. All factors were constrained to be orthogonal (i.e., factor correlations were fixed to 0). The fourth model was a hypothesis-driven bifactor model, which tested whether shared variation across measures could be explained by their anatomical categories. In this model, measures were grouped into four specific factors according to their anatomical categories. For all models, factor variances were fixed to 1 to ensure identification. Based on goodness-of-fit indices, including the highest comparative fit index (CFI) and lowest χ^2, Akaike information criterion (AIC), and standardized root mean square residual (SRMR) values, the bifactor model provided the best fit and was selected as the final model.

Gene mapping

We performed gene-level association analysis using MAGMA (version 1.08)[67] under default settings, assigning SNPs to genes using a 0 kb window. A sensitivity analysis was conducted using a ± 10 kb annotation window. The locations of protein-coding genes were obtained from NCBI Build 37. The 1000 Genomes Project phase 3 reference panel was used to calculate LD across SNPs and genes. A total of 19,110 protein-coding genes were included in the analysis. We applied a Bonferroni-corrected significance threshold of 5.23×10^{-8} (correction across 50 bone measures × 19,110 genes) to account for multiple testing.

In addition to MAGMA positional mapping, we performed functional gene mapping using the FUMA platform[128]. In FUMA, functionally annotated SNPs were mapped to genes based on three criteria: (1) physical position (window size = 10 kb), and (2) eQTL associations from GTEx muscle skeletal tissues (v6–v8), with an FDR threshold of 0.05, and (3) chromatin interaction mapping using a mesenchymal stem cells-derived osteoblasts dataset[129]. Only protein-coding genes were considered, and the MHC region was excluded from annotation. All other FUMA mapping settings were kept as default.

Enrichment analysis

MAGMA gene set analysis was used to explore the functional and biological mechanisms underlying the genetic components of the 50 bone measures. We tested 10,519 Gene Ontology (GO)[130] gene sets from the Molecular Signatures Database (MsigDB, version 2023.1Hs)[131], including sub-collections for biological process (BP), cellular

component (CC), and molecular function (MF). The gene set analysis was conducted using the default competitive model, which evaluates whether the joint association within a gene set is stronger than that observed in a randomly selected set of genes. Significant findings were reported at an FDR threshold of 5% (across 50 bone measures × 10,519 gene sets).

We also performed stratified LD score regression[68] to assess heritability enrichment for bone measures, utilizing genetic variant annotations of tissue types and cell type-specific regulatory elements from the Roadmap Epigenomics Consortium[132]. A total of 396 regulatory elements across 88 adult and fetal tissues or cell types were examined, including DNase I hypersensitivity and activating histone markers (H3K27ac, H3K4me3, H3K4me1, H3K9ac, and H3K36me3). These 88 primary tissues or cell types were organized into 19 categories based on their tissue origins. Baseline models were used in the calculation of enrichment scores for each annotation. Significant findings were reported at an FDR threshold of 5% (across 50 bone measures × 396 regulatory elements).

Global and local genetic correlations between bone and brain

We used LDSC[70] v.1.0.1 to assess pairwise genetic correlations between 50 bone measures and 70 human complex traits and disorders, encompassing psychological traits, physical conditions, and brain and musculoskeletal disorders (Supplementary Data 28). We used the pre-calculated LD scores and weights derived from the 1000 Genomes Project European samples. The analysis focused on HapMap3 variants, excluding variants located within the MHC region. Significant genetic correlations were reported at an FDR threshold of 5% (across 50 bone measures × 70 phenotypes).

We used the Local Analysis of [co] Variant Association (LAVA)[72] package to evaluate pairwise local genetic correlations between the 50 bone measures and 21 brain disorders (a subset of the 70 complex traits), as well as 488 brain measures with default settings. LAVA yields stable local genetic correlation estimates and uses a pre-defined LD-block partition that supports reproducible genome-wide exploration. Previous studies[133,134] have demonstrated that many brain disorders are highly polygenic and tend to exhibit mixed genetic correlation effects (i.e., both positive and negative correlations across different loci). We thus focused on brain disorders in this analysis. LAVA quantifies genetic correlations across 2495 semi-independent genetic loci, each approximately 1 Mb in size, enabling the detection of mixed-effect directions even when the global genetic correlation is minimal. In this study, we first conducted univariate analysis to select loci with significant local heritability for each trait ($p < 2.00 \times 10^{-5}$, corrected across 2495 genetic loci). We then conducted bivariate tests for selected loci and trait pairs to examine their local genetic correlations at the Bonferroni-corrected significance level ($p < 9.78 \times 10^{-7}$ for brain disorders, across 51,110 locus–bone–brain pairs; $p < 1.17 \times 10^{-6}$ for brain measures, across 42,737 locus–bone–brain pairs).

Polygenic risk scores

We used PRS-CS[71,135] to construct polygenic risk scores (PRS) for 50 bone measures using GWAS summary statistics from the discovery dataset. The "auto" mode of PRS-CS was used with default settings, which allowed all model parameters to be learned from data through a fully Bayesian approach, eliminating the need for a validation dataset. As a benchmark, the prediction accuracy of the bone PRS for the corresponding bone measure was assessed using incremental r^2 in the independent validation cohort of European ancestry ($N = 4720$). Specifically, for each bone measure, two linear regression models were constructed: one that included the corresponding PRS along with covariates (age, age squared, sex, sex-by-age and sex-by-age squared interactions, and the top 40 genetic PCs); the other that used only the covariates. The incremental r^2 was then calculated by subtracting the r^2 value of the covariate-only model from the r^2 value of the full model that included both covariates and PRS.

White British individuals of European ancestry in the UKB who did not have bone DXA data and were unrelated to the bone GWAS sample were used to evaluate the associations between the PRS of 50 bone measures and 204 complex phenotypes across 14 categories, including cognitive ability, education, personality, mental health, disease, pain, medical conditions, diet preferences, sleep, employment, body composition, hand grip, physical activity, and smoking or alcohol use (Supplementary Data 31). After preprocessing the phenotype data, linear regression models were used, with the complex phenotype as the dependent variable and the PRS as the independent variable of interest. Covariates in the models included age, age squared, sex, sex-by-age and sex-by-age squared interactions, and the top 40 genetic PCs. Continuous variables were standardized to facilitate interpretation. We reported significant predictions at the Bonferroni-corrected significance level ($p < 4.90 \times 10^{-6}$, across 50 bone measures × 204 complex phenotypes).

Enrichment analysis for genes related to both bone and brain

To identify genetic variants underlying both bone and brain, we searched the NHGRI-EBI GWAS Catalog[73] (version e110_r2023-07-20; https://www.ebi.ac.uk/gwas) for SNPs that are associated with both bone measures and brain-related traits and disorders. These SNPs were then mapped to genes based on their physical positions using MAGMA, resulting in the identification of 58 overlapping genes. We performed enrichment analysis on these genes using the clusterProfiler package[136] to gain deeper insights into the biological pathways underlying the bone-brain associations. This functional annotation tool allowed us to test the enrichment of GO terms across BP, MF, and CC categories, as well as the terms from the Kyoto Encyclopedia of Genes and Genomes (KEGG) pathway database[137]. Significant results were reported at an FDR threshold of 5%.

Since the SNPs used to identify overlapping genes may not represent true causal variants, fine-mapping was additionally performed to prioritize variants with higher posterior probabilities of causality. Fine-mapping was conducted for all 50 bone measures using susieR (v0.14.2) within ±1.5 Mb windows centered on the lead variant of each genomic locus[138]. Overlapping windows were merged into a single fine-mapping region. The SuSiE model was fitted using an in-sample LD matrix calculated with PLINK 2.0 from the same individuals included in the GWAS. The MHC region was excluded due to its complex LD structure. SuSiE estimated the posterior inclusion probability (PIP) for each SNP and constructed 95% credible sets, assuming a maximum of 10 causal variants per locus. SNPs located within credible sets with PIP > 0.10 and annotated as non-synonymous or untranslated region (UTR) variants were then mapped to genes. The enrichment analysis was subsequently rerun using these prioritized genes, with all parameter settings consistent with the primary analysis.

Drug query

We assessed the druggability of 17 overlapping genes between bone and brain that are involved in the canonical Wnt signaling pathway, using the Drug-Gene Interaction Database (DGIdb)[139] and Druggable Genome database[74]. Druggable genes were then mapped to candidate compounds based on target chemical information for both approved or experimental medications from DrugBank (https://go.drugbank.com) and the Therapeutic Target Database (https://idrblab.net/ttd/). To prioritize potential drugs targeting the canonical Wnt pathway-related genes in bone and brain, we utilized the Gene2Drug package[78]. This drug repositioning tool integrates curated pathway annotations with transcriptional responses to 1309 drug treatments from the Connectivity Map, and conducts gene set enrichment analysis to assess drug-induced upregulation or downregulation of pathways

involving the input gene. Drugs were considered significant if they had a Bonferroni-corrected p-value less than 2.24×10^{-6} (corrected across 1309 drugs × 17 genes) and an absolute enrichment score (EScore) greater than 0.8. For each gene, up to three predicted drugs were reported.

Colocalization of GWAS signals between bone and brain

To investigate whether overlapping genetic signals between bone measures and phenotypes identified in the NHGRI-EBI GWAS Catalog reflect shared underlying causal signals, we performed Bayesian colocalization analysis[79] using COLOC (R package, version 5.2.3). Our analysis focused on publicly available GWAS summary statistics for brain MRI measures, as well as bone and brain-related traits and disorders. GWAS with non-European samples, small sample sizes ($N < 10{,}000$), and poor data quality (e.g., lacking effect sizes or insufficient SNP counts) were excluded. For each colocalization analysis, we examined genomic regions that included all variants within a ± 250 kb window centered around the index variant for each bone measure. Phenotypes with an SNP overlap ratio less than 0.5 were excluded. COLOC evaluates five hypotheses: H0, no association with either trait; H1, bone measure association only; H2, phenotype association only; H3, associations with both traits but driven by two distinct variants; H4, associations with both traits attributable to a shared causal variant. Evidence of colocalization was defined as a posterior probability of shared causal variants (PPH4) exceeding 0.8. LocusZoom (http://locuszoom.org/) was used to generate regional plots for colocalized signals.

Mendelian randomization

We applied Mendelian Randomization (MR)[80] to evaluate the potential causal relationships between 50 bone measures and 20 brain disorders, including mental and behavioral disorders, nervous system disorders, and sleep disorders (Supplementary Data 45). With the exception of anorexia nervosa, all GWAS summary statistics of brain disorders did not overlap with individuals from the UKB. Anorexia nervosa had a 5.3% overlap with the UKB sample (3833 out of 72,517 individuals), which is unlikely to introduce significant bias into the MR analysis[140]. For each GWAS, genetic variants with a MAF less than 1% were excluded. Genome-wide significant variants were extracted from the exposure GWAS.

To ensure the independence of genetic variants included in the MR analysis, a clumping algorithm was applied with an r^2 threshold of 0.001 and a window size of 1 Mb, using the 1000 Genomes Project European samples as a reference panel. To mitigate weak instrument bias, we calculated F-statistics for all genetic variants following an established procedure[141] and only retained variants with an F-statistic > 10 in the exposure GWAS. Variants directly associated with the outcomes were removed to avoid potential horizontal pleiotropy. The effects of genetic variants on both exposure and outcome were aligned to the same alleles. Palindromic variants with MAF greater than 0.42 were excluded. Outliers were identified and removed using the "ivw_radial" (alpha = 0.05, weights = 1, to l = 0.0001) and "egger_radial" (alpha = 0.05, weights = 1) functions from the "RadialMR" package[142]. The remaining variants were used as instrumental variables (IVs) for the MR analysis.

We conducted bidirectional two-sample MR analyses using the TwoSampleMR package (https://mrcieu.github.io/TwoSampleMR). The fixed-effect inverse variance weighted (IVW) method was used for exposures with two or three IVs, while the multiplicative random-effects IVW method was used for exposures with more than three IVs. To minimize the risk of violating MR assumptions, exposures with a single IV were excluded from the analysis. To assess the robustness of the IVW estimates, we performed secondary analyses using nine additional MR methods: MR-Egger, MR-RAPs, simple median, weighted median, penalized weighted median, simple mode, simple mode (NOME), weighted mode, and weighted mode (NOME) method. Causal effects were considered significant if they reached Bonferroni-corrected significance ($p < 5 \times 10^{-5}$ for bone exposures; $p < 6.68 \times 10^{-5}$ for bone outcomes) in the IVW analyses, reached nominal significance ($p < 0.05$) in at least one of the secondary MR methods, and demonstrated consistent effect directions across all methods.

Given that bone–brain relationships may involve multiple biological pathways, we applied multivariable Mendelian randomization (MVMR) to estimate the direct causal effect of bone traits on brain outcomes independent of metabolic, inflammatory, or gut microbiota factors[143–145]. For each significant univariable MR association, we first examined whether potential biological confounders (1091 metabolic, 91 inflammatory, and 257 gut microbiota factors) causally influenced the outcome using the same two-sample MR procedure. Any factor showing a significant association was included as a secondary exposure in the MVMR model. When IVs for the primary exposure were missing in the GWAS summary statistics of the secondary exposure or outcome, we used high-LD proxy SNPs ($r^2 > 0.8$) to retain instrument availability. MVMR analyses were performed using the MV-IVW method implemented in the MendelianRandomization R package (0.10.0), which accounts for correlations among exposures. There was no sample overlap between the GWAS datasets of the biological factors and those for the bone measures or brain disorders.

Data availability

GWAS summary statistics and polygenic risk score weights generated from the current study are deposited on Zenodo (10.5281/zenodo.17966320). Summary statistics of brain measures for genetic correlation analyses were obtained from the BIG40 dataset (https://open.win.ox.ac.uk/ukbiobank/big40/). Summary statistics of brain traits and disorders used in genetic correlation and Mendelian Randomization analyses are summarized in Supplementary Data 28 and 45. Spatial distribution maps of cortical microarchitecture, evolution patterns, and AHBA genes used in the current study are summarized in Supplementary Data 6. The individual-level data used in the current study, including imaging, genetic and phenotypic data, were obtained from the UKB (https://www.ukbiobank.ac.uk/; application number 71901) and are available upon application to the UKB. All other data supporting the findings of this study are available within the article and its Supplementary Data files.

Code availability

All software and methods used in this study are publicly available and described in the Methods section. Custom analysis code is available at https://github.com/tulab-brain/Bone-Brain-connections/.

References

1. Biewener, A. A. Biomechanics of mammalian terrestrial locomotion. *Science* **250**, 1097–1103 (1990).
2. Morrison, S. J. & Scadden, D. T. The bone marrow niche for haematopoietic stem cells. *Nature* **505**, 327–334 (2014).
3. Murshed, M. Mechanism of bone mineralization. *Cold Spring Harb. Perspect. Med.* **8**, a031229 (2018).
4. Weaver, C. M. & Peacock, M. Calcium. *Adv. Nutr.* **10**, 546–548 (2019).
5. Lee, N. K. et al. Endocrine regulation of energy metabolism by the skeleton. *Cell* **130**, 456–469 (2007).
6. Karsenty, G. & Ferron, M. The contribution of bone to whole-organism physiology. *Nature* **481**, 314–320 (2012).
7. Ma, C. et al. Autonomic neural regulation in mediating the brain–bone axis: mechanisms and implications for regeneration under psychological stress. *QJM* **117**, 95–108 (2024).
8. Liu, J. et al. Wnt/β-catenin signalling: function, biological mechanisms, and therapeutic opportunities. *Signal Transduct. Target Ther.* **7**, 3 (2022).

9. Hu, L., Chen, W., Qian, A. & Li, Y.-P. Wnt/β-catenin signaling components and mechanisms in bone formation, homeostasis, and disease. *Bone Res.* **12**, 39 (2024).
10. Hussaini, S. M. Q. et al. Wnt signaling in neuropsychiatric disorders: ties with adult hippocampal neurogenesis and behavior. *Neurosci. Biobehav. Rev.* **47**, 369–383 (2014).
11. Lv, X., Gao, F. & Cao, X. Skeletal interoception in bone homeostasis and pain. *Cell Metab.* **34**, 1914–1931 (2022).
12. Chen, H. et al. Prostaglandin E2 mediates sensory nerve regulation of bone homeostasis. *Nat. Commun.* **10**, 181 (2019).
13. Babey, M. E. et al. A maternal brain hormone that builds bone. *Nature* **632**, 357–365 (2024).
14. Zhang, L. et al. Bidirectional control of parathyroid hormone and bone mass by subfornical organ. *Neuron* **111**, 1914–1932.e6 (2023).
15. Shi, T. et al. Osteocyte-derived sclerostin impairs cognitive function during ageing and Alzheimer's disease progression. *Nat. Metab.* **6**, 531–549 (2024).
16. Oury, F. et al. Maternal and offspring pools of osteocalcin influence brain development and functions. *Cell* **155**, 228–241 (2013).
17. Schini, M. et al. Increased fracture risk in Parkinson's disease—an exploration of mechanisms and consequences for fracture prediction with FRAX. *Bone* **168**, 116651 (2023).
18. Lee, C. W.-S. et al. Increased risk of osteoporosis in patients with depression: a population-based retrospective cohort study. *Mayo Clin. Proc.* **90**, 63–70 (2015).
19. Chang, K.-H. et al. Increased risk of dementia in patients with osteoporosis: a population-based retrospective cohort analysis. *Age* **36**, 967–975 (2014).
20. Lin, C.-H. et al. A population-based five-year study on the risk of stroke in patients with osteoporosis in Taiwan. *Bone* **72**, 9–13 (2015).
21. Zhao, Y., Chen, H., Qiu, F., He, J. & Chen, J. Cognitive impairment and risks of osteoporosis: a systematic review and meta-analysis. *Arch. Gerontol. Geriatr.* **106**, 104879 (2023).
22. Weber, A. et al. Association between osteoarthritis and increased risk of dementia: a systemic review and meta-analysis. *Medicines* **98**, e14355 (2019).
23. Yen, C.-M. et al. Sleep disorders increase the risk of osteoporosis: a nationwide population-based cohort study. *Sleep. Med.* **15**, 1339–1344 (2014).
24. Kun, E. et al. The genetic architecture and evolution of the human skeletal form. *Science* **381**, eadf8009 (2023).
25. Lindhout, F. W., Krienen, F. M., Pollard, K. S. & Lancaster, M. A. A molecular and cellular perspective on human brain evolution and tempo. *Nature* **630**, 596–608 (2024).
26. Johnson, M. A., Polgar, J., Weightman, D. & Appleton, D. Data on the distribution of fibre types in thirty-six human muscles. An autopsy study. *J. Neurol. Sci.* **18**, 111–129 (1973).
27. Watson, E. C. & Adams, R. H. Biology of bone: the vasculature of the skeletal system. *Cold Spring Harb. Perspect. Med.* **8**, a031559 (2018).
28. Tomlinson, R. E. & Silva, M. J. Skeletal blood flow in bone repair and maintenance. *Bone Res* **1**, 311–322 (2013).
29. Elefteriou, F. Impact of the autonomic nervous system on the skeleton. *Physiol. Rev.* **98**, 1083–1112 (2018).
30. Tei, R. M. H., Ramlau-Hansen, C. H., Plana-Ripoll, O., Brink, O. & Langdahl, B. L. OFELIA: prevalence of osteoporosis in fragility fracture patients. *Calcif. Tissue Int* **104**, 102–114 (2019).
31. GBD 2021 Osteoarthritis Collaborators Global, regional, and national burden of osteoarthritis, 1990–2020 and projections to 2050: a systematic analysis for the Global Burden of Disease Study 2021. *Lancet Rheumatol.* **5**, e508–e522 (2023).
32. Bernier, M., Cunnane, S. C. & Whittingstall, K. The morphology of the human cerebrovascular system. *Hum. Brain Mapp.* **39**, 4962–4975 (2018).
33. Wilhelm, I., Nyúl-Tóth, Á, Suciu, M., Hermenean, A. & Krizbai, I. A. Heterogeneity of the blood-brain barrier. *Tissue Barriers* **4**, e1143544 (2016).
34. Shafiei, G. et al. Neurophysiological signatures of cortical microarchitecture. *Nat. Commun.* **14**, 6000 (2023).
35. Ulrich-Lai, Y. M. & Herman, J. P. Neural regulation of endocrine and autonomic stress responses. *Nat. Rev. Neurosci.* **10**, 397–409 (2009).
36. Rao, Y. L. et al. Hippocampus and its involvement in Alzheimer's disease: a review. *3 Biotech* **12**, 55 (2022).
37. McGregor, M. M. & Nelson, A. B. Circuit mechanisms of Parkinson's disease. *Neuron* **101**, 1042–1056 (2019).
38. McCutcheon, R. A. et al. Shared and separate patterns in brain morphometry across transdiagnostic dimensions. *Nat. Ment. Health* **1**, 55–65 (2023).
39. Smith, S. M. et al. An expanded set of genome-wide association studies of brain imaging phenotypes in UK Biobank. *Nat. Neurosci.* **24**, 737–745 (2021).
40. Morris, J. A. et al. An atlas of genetic influences on osteoporosis in humans and mice. *Nat. Genet.* **51**, 258–266 (2019).
41. Warrier, V. et al. Genetic insights into human cortical organization and development through genome-wide analyses of 2347 neuroimaging phenotypes. *Nat. Genet.* **55**, 1483–1493 (2023).
42. Satizabal, C. L. et al. Genetic architecture of subcortical brain structures in 38,851 individuals. *Nat. Genet* **51**, 1624–1636 (2019).
43. Zhao, B. et al. Common genetic variation influencing human white matter microstructure. *Science* **372**, eabf3736 (2021).
44. Chen, X. et al. Kidney damage causally affects the brain cortical structure: a Mendelian randomization study. *EBioMedicine* **72**, 103592 (2021).
45. Liao, G.-Z. et al. Exploring the heart-brain and brain-heart axes: Insights from a bidirectional Mendelian randomization study on brain cortical structure and cardiovascular disease. *Neurobiol. Dis.* **200**, 106636 (2024).
46. Lin, S. et al. Inferring the genetic relationship between brain imaging-derived phenotypes and risk of complex diseases by Mendelian randomization and genome-wide colocalization. *Neuroimage* **279**, 120325 (2023).
47. Bycroft, C. et al. The UK Biobank resource with deep phenotyping and genomic data. *Nature* **562**, 203–209 (2018).
48. Naik, A., Kale, A. A. & Rajwade, J. M. Sensing the future: a review on emerging technologies for assessing and monitoring bone health. *Biomater. Adv.* **165**, 214008 (2024).
49. Ensrud, K. E. & Crandall, C. J. Osteoporosis. *Ann. Intern. Med.* **167**, ITC17–ITC32 (2017).
50. Ellis, K. J. Human body composition: in vivo methods. *Physiol. Rev.* **80**, 649–680 (2000).
51. Zhang, F. et al. Secretin-dependent signals in the ventromedial hypothalamus regulate energy metabolism and bone homeostasis in mice. *Nat. Commun.* **15**, 1030 (2024).
52. Yang, F. et al. A GABAergic neural circuit in the ventromedial hypothalamus mediates chronic stress–induced bone loss. *J. Clin. Investig.* **130**, 6539–6554 (2020).
53. Nieves, J. W. Sex-differences in skeletal growth and aging. *Curr. Osteoporos. Rep.* **15**, 70–75 (2017).
54. Ruigrok, A. N. V. et al. A meta-analysis of sex differences in human brain structure. *Neurosci. Biobehav Rev.* **39**, 34–50 (2014).
55. Markello, R. D. et al. neuromaps: structural and functional interpretation of brain maps. *Nat. Methods* **19**, 1472–1479 (2022).
56. Hansen, J. Y. et al. Mapping neurotransmitter systems to the structural and functional organization of the human neocortex. *Nat. Neurosci.* **25**, 1569–1581 (2022).
57. Burt, J. B., Helmer, M., Shinn, M., Anticevic, A. & Murray, J. D. Generative modeling of brain maps with spatial autocorrelation. *Neuroimage* **220**, 117038 (2020).

58. Bethlehem, R.aI. et al. Brain charts for the human lifespan. *Nature* **604**, 525–533 (2022).
59. Berendsen, A. D. & Olsen, B. R. Bone development. *Bone* **80**, 14–18 (2015).
60. Zheng, H.-F. et al. Whole-genome sequencing identifies EN1 as a determinant of bone density and fracture. *Nature* **526**, 112–117 (2015).
61. Medina-Gomez, C. et al. Life-course genome-wide association study meta-analysis of total body BMD and assessment of age-specific effects. *Am. J. Hum. Genet.* **102**, 88–102 (2018).
62. Kemp, J. P. et al. Identification of 153 new loci associated with heel bone mineral density and functional involvement of GPC6 in osteoporosis. *Nat. Genet.* **49**, 1468–1475 (2017).
63. Qian, Y. et al. Genome-wide association studies of over 30,000 samples with bone mineral density at multiple skeletal sites and its clinical relevance. *Genom. Proteomics Bioinform.* **23**, qzaf097 (2025).
64. Bulik-Sullivan, B. K. et al. LD Score regression distinguishes confounding from polygenicity in genome-wide association studies. *Nat. Genet.* **47**, 291–295 (2015).
65. Yang, J., Lee, S. H., Goddard, M. E. & Visscher, P. M. GCTA: a tool for genome-wide complex trait analysis. *Am. J. Hum. Genet.* **88**, 76–82 (2011).
66. Grotzinger, A. D. et al. Genomic structural equation modelling provides insights into the multivariate genetic architecture of complex traits. *Nat. Hum. Behav.* **3**, 513–525 (2019).
67. Leeuw, C. A. de, Mooij, J. M., Heskes, T. & Posthuma, D. MAGMA: generalized gene-set analysis of GWAS data. *PLOS Comput. Biol.* **11**, e1004219 (2015).
68. Finucane, H. K. et al. Heritability enrichment of specifically expressed genes identifies disease-relevant tissues and cell types. *Nat. Genet.* **50**, 621–629 (2018).
69. Otto, E. et al. Crosstalk of brain and bone—clinical observations and their molecular bases. *Int. J. Mol. Sci.* **21**, 4946 (2020).
70. Bulik-Sullivan, B. et al. An atlas of genetic correlations across human diseases and traits. *Nat. Genet.* **47**, 1236–1241 (2015).
71. Kachuri, L. et al. Principles and methods for transferring polygenic risk scores across global populations. *Nat. Rev. Genet* **25**, 8–25 (2024).
72. Werme, J., van der Sluis, S., Posthuma, D. & de Leeuw, C. A. An integrated framework for local genetic correlation analysis. *Nat. Genet.* **54**, 274–282 (2022).
73. Buniello, A. et al. The NHGRI-EBI GWAS Catalog of published genome-wide association studies, targeted arrays and summary statistics 2019. *Nucleic Acids Res.* **47**, D1005–D1012 (2019).
74. Finan, C. et al. The druggable genome and support for target identification and validation in drug development. *Sci. Transl. Med.* **9**, eaag1166 (2017).
75. Visanji, N. P. et al. PYM50028, a novel, orally active, nonpeptide neurotrophic factor inducer, prevents and reverses neuronal damage induced by MPP+ in mesencephalic neurons and by MPTP in a mouse model of Parkinson's disease. *FASEB J.* **22**, 2488–2497 (2008).
76. Wen, Y. et al. Efficacy and safety of perioperative application of esketamine on postoperative depression: a meta-analysis of randomized controlled studies. *Int. J. Surg.* **111**, 1191–1202 (2025).
77. Rousseau, J.-C. & Delmas, P. D. Biological markers in osteoarthritis. *Nat. Clin. Pract. Rheumatol.* **3**, 346–356 (2007).
78. Napolitano, F. et al. gene2drug: a computational tool for pathway-based rational drug repositioning. *Bioinformatics* **34**, 1498–1505 (2018).
79. Giambartolomei, C. et al. Bayesian test for colocalisation between pairs of genetic association studies using summary statistics. *PLOS Genet.* **10**, e1004383 (2014).
80. Hemani, G. et al. The MR-Base platform supports systematic causal inference across the human phenome. *Elife* **7**, e34408 (2018).
81. Sanderson, E., Spiller, W. & Bowden, J. Testing and correcting for weak and pleiotropic instruments in two-sample multivariable Mendelian Randomization. *Stat. Med.* **40**, 5434–5452 (2021).
82. Tang, Y., Wang, Z., Cao, J. & Tu, Y. Bone–brain crosstalk in osteoarthritis: pathophysiology and interventions. *Trends Mol. Med.* **31**, 281–295 (2025).
83. Zhang, F. & Zhang, W. Research progress in Alzheimer's disease and bone-brain axis. *Ageing Res. Rev.* **98**, 102341 (2024).
84. Khrimian, L. et al. Gpr158 mediates osteocalcin's regulation of cognition. *J. Exp. Med.* **214**, 2859–2873 (2017).
85. Abe, E. et al. TSH is a negative regulator of skeletal remodeling. *Cell* **115**, 151–162 (2003).
86. Zaidi, M., Yuen, T. & Kim, S.-M. Pituitary crosstalk with bone, adipose tissue and brain. *Nat. Rev. Endocrinol.* **19**, 708–721 (2023).
87. Saper, C. B. & Lowell, B. B. The hypothalamus. *Curr. Biol.* **24**, R1111–R1116 (2014).
88. Gonda, X., Tarazi, F. I. & Dome, P. The emergence of antidepressant drugs targeting GABAA receptors: a concise review. *Biochem Pharm.* **228**, 116481 (2024).
89. Korpi, E. R. & Sinkkonen, S. T. GABA(A) receptor subtypes as targets for neuropsychiatric drug development. *Pharm. Ther.* **109**, 12–32 (2006).
90. Pourhamzeh, M. et al. The roles of serotonin in neuropsychiatric disorders. *Cell Mol. Neurobiol.* **42**, 1671–1692 (2022).
91. Wu, Q., He, Q., Zhang, X., Chen, S. & Xue, X. Systemic modulators: potential mechanism for the 5-HT system to mediate exercise amelioration in Alzheimer's disease. *Aging Dis.* **16**, 2770–2802 (2024).
92. Yadav, V. K. et al. A serotonin-dependent mechanism explains the leptin regulation of bone mass, appetite, and energy expenditure. *Cell* **138**, 976–989 (2009).
93. Obri, A., Khrimian, L., Karsenty, G. & Oury, F. Osteocalcin in the brain: from embryonic development to age-related decline in cognition. *Nat. Rev. Endocrinol.* **14**, 174–182 (2018).
94. Rakic, P. A small step for the cell, a giant leap for mankind: a hypothesis of neocortical expansion during evolution. *Trends Neurosci.* **18**, 383–388 (1995).
95. Hofer, E. et al. Genetic correlations and genome-wide associations of cortical structure in general population samples of 22,824 adults. *Nat. Commun.* **11**, 4796 (2020).
96. Cox, S. R. et al. Ageing and brain white matter structure in 3513 UK Biobank participants. *Nat. Commun.* **7**, 13629 (2016).
97. Styrkarsdottir, U. et al. Sequence variants in the PTCH1 gene associate with spine bone mineral density and osteoporotic fractures. *Nat. Commun.* **7**, 10129 (2016).
98. Chesi, A. et al. A genomewide association study identifies two sex-specific loci, at SPTB and IZUMO3, influencing pediatric bone mineral density at multiple skeletal sites. *J. Bone Min. Res.* **32**, 1274–1281 (2017).
99. Bae, I.-S., Kim, J. M., Cheong, J. H., Ryu, J. I. & Han, M.-H. Association between bone mineral density and brain parenchymal atrophy and ventricular enlargement in healthy individuals. *Aging* **11**, 8217–8238 (2019).
100. Ruggiero, C. et al. Dementia, osteoporosis and fragility fractures: intricate epidemiological relationships, plausible biological connections, and twisted clinical practices. *Ageing Res. Rev.* **93**, 102130 (2024).
101. Chandrasekaran, V. et al. Bipolar disorder and bone health: a systematic review. *J. Affect Disord.* **249**, 262–269 (2019).
102. Zhu, B. et al. Total bone mineral density is inversely associated with stroke: a family osteoporosis cohort study in rural China. *QJM* **115**, 228–234 (2022).

103. Xiao, T. et al. Association of bone mineral density and dementia: the Rotterdam study. *Neurology* **100**, e2125–e2133 (2023).
104. Foertsch, S. et al. Chronic psychosocial stress disturbs long-bone growth in adolescent mice. *Dis. Model Mech.* **10**, 1399–1409 (2017).
105. Tsao, H. M. et al. Association of bone turnover markers and craving reduction in patients with alcohol use disorder during withdrawal: exploring the role of bone-brain axis. *Alcohol Clin. Exp. Res.* **48**, 2294–2302 (2024).
106. Lam, R. W. et al. Fluoxetine improves bone microarchitecture and mechanical properties in rodents undergoing chronic mild stress – an animal model of depression. *Transl. Psychiatry* **12**, 1–9 (2022).
107. Gupta, D. P. et al. Knee osteoarthritis accelerates amyloid beta deposition and neurodegeneration in a mouse model of Alzheimer's disease. *Mol. Brain* **16**,(2023).
108. Baron, R. & Kneissel, M. WNT signaling in bone homeostasis and disease: from human mutations to treatments. *Nat. Med* **19**, 179–192 (2013).
109. Oliva, C. A., Vargas, J. Y. & Inestrosa, N. C. Wnt signaling: role in LTP, neural networks and memory. *Ageing Res. Rev.* **12**, 786–800 (2013).
110. Dengler-Crish, C. M., Ball, H. C., Lin, L., Novak, K. M. & Cooper, L. N. Evidence of Wnt/β-catenin alterations in brain and bone of a tauopathy mouse model of Alzheimer's disease. *Neurobiol. Aging* **67**, 148–158 (2018).
111. Lorzadeh, S., Kohan, L., Ghavami, S. & Azarpira, N. Autophagy and the Wnt signaling pathway: a focus on Wnt/β-catenin signaling. *Biochim. Biophys. Acta Mol. Cell Res.* **1868**, 118926 (2021).
112. Wang, C. S., Kavalali, E. T. & Monteggia, L. M. BDNF signaling in context: from synaptic regulation to psychiatric disorders. *Cell* **185**, 62–76 (2022).
113. Merighi, A. Brain-derived neurotrophic factor, nociception, and pain. *Biomolecules* **14**, 539 (2024).
114. Park, E. J., Truong, V.-L., Jeong, W.-S. & Min, W.-K. Brain-Derived Neurotrophic Factor (BDNF) enhances osteogenesis and may improve bone microarchitecture in an ovariectomized rat model. *Cells* **13**, 518 (2024).
115. Klein, A. & Tourville, J. 101 labeled brain images and a consistent human cortical labeling protocol. *Front. Neurosci.* **6**, 171 (2012).
116. Patenaude, B., Smith, S. M., Kennedy, D. N. & Jenkinson, M. A Bayesian model of shape and appearance for subcortical brain segmentation. *Neuroimage* **56**, 907–922 (2011).
117. Mori, S. et al. Stereotaxic white matter atlas based on diffusion tensor imaging in an ICBM template. *Neuroimage* **40**, 570–582 (2008).
118. Karczewski, K. J. et al. Pan-UK Biobank genome-wide association analyses enhance discovery and resolution of ancestry-enriched effects. *Nat. Genet.* **57**, 2408–2417 (2025).
119. Zhang, Y. et al. Purification and characterization of progenitor and mature human astrocytes reveals transcriptional and functional differences with mouse. *Neuron* **89**, 37–53 (2016).
120. Lake, B. B. et al. Integrative single-cell analysis of transcriptional and epigenetic states in the human adult brain. *Nat. Biotechnol.* **36**, 70–80 (2018).
121. Habib, N. et al. Massively parallel single-nucleus RNA-seq with DroNc-seq. *Nat. Methods* **14**, 955–958 (2017).
122. Darmanis, S. et al. A survey of human brain transcriptome diversity at the single cell level. *Proc. Natl. Acad. Sci. USA* **112**, 7285–7290 (2015).
123. Li, M. et al. Integrative functional genomic analysis of human brain development and neuropsychiatric risks. *Science* **362**, eaat7615 (2018).
124. Seidlitz, J. et al. Transcriptomic and cellular decoding of regional brain vulnerability to neurogenetic disorders. *Nat. Commun.* **11**, 3358 (2020).
125. Hawrylycz, M. J. et al. An anatomically comprehensive atlas of the adult human brain transcriptome. *Nature* **489**, 391–399 (2012).
126. Markello, R. D. et al. Standardizing workflows in imaging transcriptomics with the abagen toolbox. *Elife* **10**, e72129 (2021).
127. Mbatchou, J. et al. Computationally efficient whole-genome regression for quantitative and binary traits. *Nat. Genet.* **53**, 1097–1103 (2021).
128. Watanabe, K., Taskesen, E., van Bochoven, A. & Posthuma, D. Functional mapping and annotation of genetic associations with FUMA. *Nat. Commun.* **8**, 1826 (2017).
129. Chesi, A. et al. Genome-scale Capture C promoter interactions implicate effector genes at GWAS loci for bone mineral density. *Nat. Commun.* **10**, 1260 (2019).
130. Ashburner, M. et al. Gene ontology: tool for the unification of biology. The Gene Ontology Consortium. *Nat. Genet.* **25**, 25–29 (2000).
131. Liberzon, A. et al. The Molecular Signatures Database (MSigDB) Hallmark Gene Set Collection. *Cell Syst.* **1**, 417–425 (2015).
132. Kundaje, A. et al. Integrative analysis of 111 reference human epigenomes. *Nature* **518**, 317–330 (2015).
133. Hindley, G. et al. Charting the landscape of genetic overlap between mental disorders and related traits beyond genetic correlation. *Am. J. Psychiatry* **179**, 833–843 (2022).
134. Zhang, R. et al. Associations of dietary patterns with brain health from behavioral, neuroimaging, biochemical and genetic analyses. *Nat. Ment. Health* **2**, 535–552 (2024).
135. Ge, T. et al. Polygenic prediction via Bayesian regression and continuous shrinkage priors. *Nat. Commun.* **10**, 1776 (2019).
136. Yu, G., Wang, L.-G., Han, Y. & He, Q.-Y. clusterProfiler: an R package for comparing biological themes among gene clusters. *OMICS J. Integr. Biol.* **16**, 284–287 (2012).
137. Kanehisa, M., Furumichi, M., Sato, Y., Kawashima, M. & Ishiguro-Watanabe, M. KEGG for taxonomy-based analysis of pathways and genomes. *Nucleic Acids Res.* **51**, D587–D592 (2023).
138. Wang, G., Sarkar, A., Carbonetto, P. & Stephens, M. A simple new approach to variable selection in regression, with application to genetic fine mapping. *J. R. Stat. Soc. Ser. B Stat. Methodol.* **82**, 1273–1300 (2020).
139. Cannon, M. et al. DGIdb 5.0: rebuilding the drug-gene interaction database for precision medicine and drug discovery platforms. *Nucleic Acids Res.* **52**, D1227–D1235 (2024).
140. Burgess, S., Davies, N. M. & Thompson, S. G. Bias due to participant overlap in two-sample Mendelian randomization. *Genet. Epidemiol.* **40**, 597–608 (2016).
141. Guo, J. et al. Mendelian randomization analyses support causal relationships between brain imaging-derived phenotypes and risk of psychiatric disorders. *Nat. Neurosci.* **25**, 1519–1527 (2022).
142. Bowden, J. et al. Improving the visualization, interpretation and analysis of two-sample summary data Mendelian randomization via the Radial plot and Radial regression. *Int. J. Epidemiol.* **47**, 2100 (2018).
143. Kurilshikov, A. et al. Large-scale association analyses identify host factors influencing human gut microbiome composition. *Nat. Genet.* **53**, 156–165 (2021).
144. Zhao, J. H. et al. Genetics of circulating inflammatory proteins identifies drivers of immune-mediated disease risk and therapeutic targets. *Nat. Immunol.* **24**, 1540–1551 (2023).
145. Chen, Y. et al. Genomic atlas of the plasma metabolome prioritizes metabolites implicated in human diseases. *Nat. Genet.* **55**, 44–53 (2023).

Acknowledgements

This research was conducted using the UKB resource under application 71901. We thank UKB participants and the UKB research teams for their work on collecting, processing, and disseminating these datasets for

analysis. We are grateful to all authors and institutions that made gene expression, cortical annotations, and GWAS summary-level data publicly available. This work was supported by National Natural Science Foundation of China (32322035, 32171078), the Scientific Foundation of the Institute of Psychology, Chinese Academy of Sciences (E0CX5210, E2CX4015), and Young Elite Scientist Sponsorship Program by the China Association for Science and Technology (E1KX0210).

Author contributions

Y.H.T. and T.G. conceived and designed this study; L.Z., Y.L.T., W.H.Z., S.J.N.L., and J.C. analyzed and interpreted the data; L.Z., Y.L.T., Y.H.T., and T.G. drafted the manuscript; Y.H.T. and T.G. supervised the project. All authors edited and contributed to the final version of the manuscript. All authors read and approved the final manuscript.

Competing interests

The authors declare no competing interests.

Additional information

Supplementary information The online version contains supplementary material available at https://doi.org/10.1038/s41467-026-73428-y.

Correspondence and requests for materials should be addressed to Tian Ge or Yiheng Tu.

Peer review information *Nature Communications* thanks Hou-Feng Zheng, and the other, anonymous, reviewer(s) for their contribution to the peer review of this work. A peer review file is available.